J. Fluid Mech. (2000), *vol.* 413, *pp.* 181–217. Printed in the United Kingdom

Breaking and broadening of internal solitary waves

By JOHN GRUE, ATLE JENSEN, PER-OLAV RUSÅS AND J. KRISTIAN SVEEN

Mechanics Division, Department of Mathematics, University of Oslo, Blinden, N-0316, Norway

(Received 26 February 1999 and in revised form 27 January 2000)

Solitary waves propagating horizontally in a stratified fluid are investigated. The fluid has a shallow layer with linear stratification and a deep layer with constant density. The investigation is both experimental and theoretical. Detailed measurements of the velocities induced by the waves are facilitated by particle tracking velocimetry (PTV) and particle image velocimetry (PIV). Particular attention is paid to the role of wave breaking which is observed in the experiments. Incipient breaking is found to take place for moderately large waves in the form of the generation of vortices in the leading part of the waves. The maximal induced fluid velocity close to the free surface is then about 80% of the wave speed, and the wave amplitude is about half of the depth of the stratified layer. Wave amplitude is defined as the maximal excursion of the stratified layer. The breaking increases in power with increasing wave amplitude. The magnitude of the induced fluid velocity in the large waves is found to be approximately bounded by the wave speed. The breaking introduces a broadening of the waves. In the experiments a maximal amplitude and speed of the waves are obtained. A theoretical fully nonlinear two-layer model is developed in parallel with the experiments. In this model the fluid motion is assumed to be steady in a frame of reference moving with the wave. The Brunt-Väisälä frequency is constant in the layer with linear stratification and zero in the other. A mathematical solution is obtained by means of integral equations. Experiments and theory show good agreement up to breaking. An approximately linear relationship between the wave speed and amplitude is found both in the theory and the experiments and also when wave breaking is observed in the latter. The upper bound of the fluid velocity and the broadening of the waves, observed in the experiments, are not predicted by the theory, however. There was always found to be excursion of the solitary waves into the layer with constant density, irrespective of the ratio between the depths of the layers.

1. Introduction

Internal waves in the ocean share many properties with ocean surface waves. However, in many respects internal waves differ fundamentally from ocean waves. Internal waves have been studied less than their counterparts on the free surface, but are now receiving increased attention for several reasons. Examples include marine activity in deep water regions where internal waves may frequently occur. Such activity may be the extraction of minerals or hydrocarbons on or below the sea bed. Compliant offshore units floating on the sea surface, like platforms or ships, may be connected to equipment and wells at the sea bottom by risers or cables. The concern is the possible loads on and vibrations of the risers and cables induced by

internal waves. A similar concern relates to submerged floating tunnels if there is a thermocline at their location. Such tunnels are under consideration for use as tunnels for cars at several places worldwide.

Several fundamental aspects of internal waves still lack satisfactory explanation. These include their generation mechanisms, propagation properties and break-up at a shore. Another aspect is mass transport in the ocean that may be induced by internal waves, which is the subject of the present study. Wave-induced mass transport has applications e.g. within geology or biology, in connection with the motion of sediments or larvae in the ocean. Some recent developments in the study of internal solitary waves, their effects and applications, may be found in Duda & Farmer (1998).

We here focus on solitary waves of mode 1 propagating horizontally in a stratified fluid. The investigation combines experiments and theory. The experiments are performed in a wave tank where the fluid has a shallow layer with linear stratification above or below a deep layer of constant density. Most of the experiments are performed with the linearly stratified fluid overlying the homogeneous fluid. The shape of the density profile is motivated by conditions in nature where solitary waves are observed, see figure 1. We generate solitary waves of mode 1 which propagate along the wave tank, see figure 2. The amplitude of the waves, defined by the maximal excursion of the stratified layer, covers a rather large range. Particle tracking velocimetry (PTV) and particle image velocimetry (PIV) are employed to make detailed recordings of the induced velocities due to the waves.

Particular attention is paid to the role of the breaking of the waves observed in the experiments. The solitary waves under consideration induce fluid velocities in the stratified layer with a magnitude that becomes comparable to the wave speed. This is true even for moderately large waves, and means that breaking will most likely occur. This represents fundamentally different dynamics from that in a two-layer fluid with homogeneous layers, where the induced fluid velocity is always significantly less than the wave speed. Surprisingly, we shall find that wave breaking occurs for rather moderate amplitude. The breaking takes place through the formation of small vortices in the leading part of the waves (for illustration, see e.g. figure 13). For large waves, intensive breaking takes place in the linearly stratified layer in the middle of the wave. The wave breaking limits the fluid velocity induced by the waves. An upper bound is found to be approximately the wave speed. The breaking also introduces a broadening of the waves.

With the purpose of interpreting the experimental results we develop a theoretical model of the waves. We consider steady wave solutions in a two-layer fluid. The Brunt–Väisälä frequency is constant in the linearly stratified layer and zero in the other. The theoretical model does not include transient effects like wave breaking. The basic equations of the fully nonlinear model are derived along the lines of previous studies (Long 1958; Yih 1960; Tung, Chan & Kubota 1982; Turkington, Eydeland & Wang 1991). The mathematical problem is solved by means of integral equations. This solution procedure is well suited to the present two-layer model, where the Brunt–Väisälä frequency is discontinuous at the transition between the two layers. The present mathematical model has much in common with an integral method for a two-layer fluid with constant density in each of the layers (Grue *et al.* 1997, 1999), and may be extended to study the transient development of the waves. We compare several quantities from the experiments with the theoretical model, including the vorticity induced by the waves. The effect of wave breaking is clearly seen in the measured vorticity, particularly when compared with the model, where wave breaking is not included.

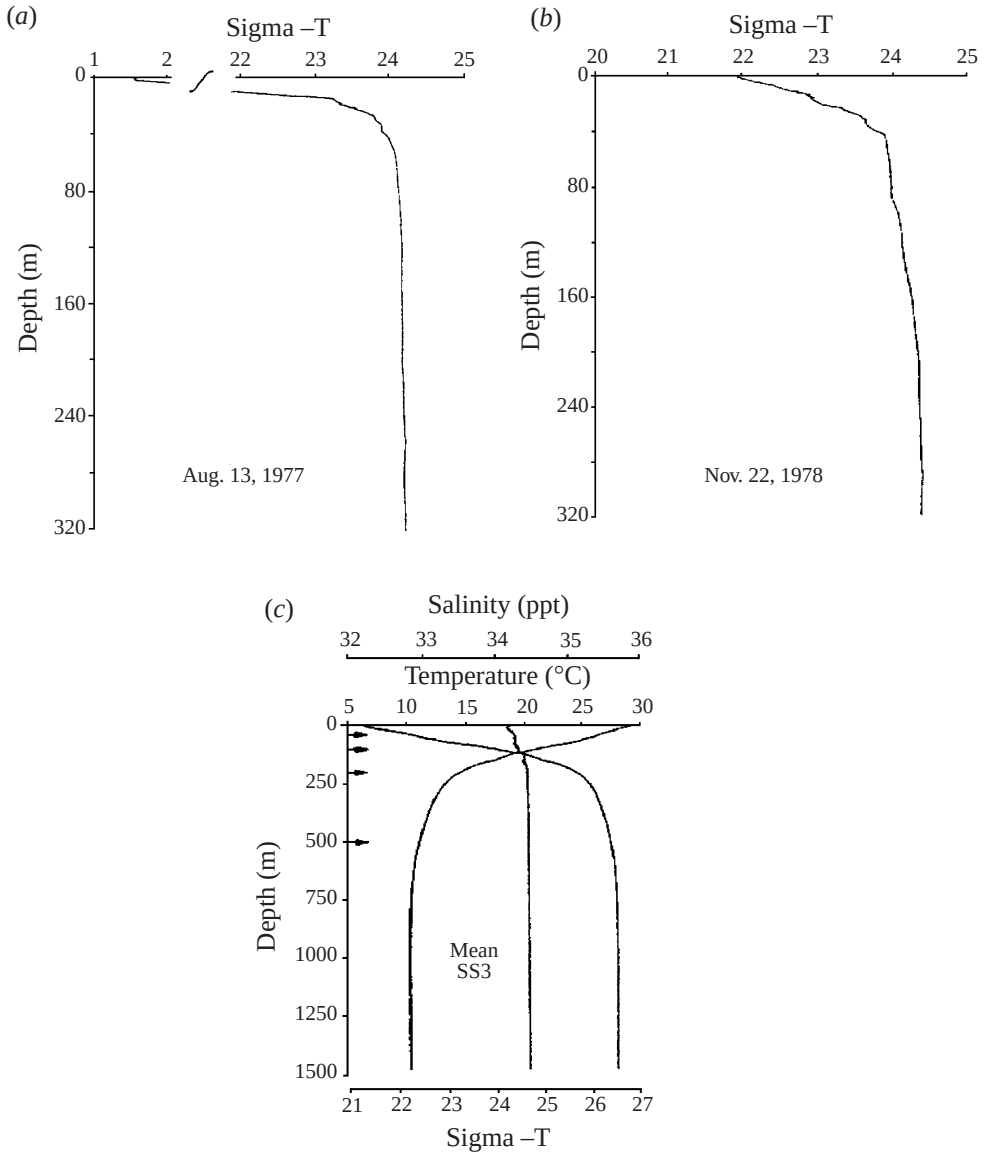

FIGURE 1. Examples of density profiles in large scale where internal solitary waves are observed. (*a*) and (*b*) At the Knight Inlet, reprinted from *Deep-Sea Res.* **27A**, Farmer, D. M. & Smith, J. D., Tidal interaction of stratified flow with a sill in Knight Inlet, p. 239, figure 2, Copyright (1980), with permission from Elsevier Science. (*c*) In the Sulu Sea (Apel *et al.* 1985, figure 3), reprinted from *J. Phys. Oceanogr.*, **15**.

If the mode 1 solitary waves are reflected in the (flat) ocean surface or the fluid bed, we obtain solitary waves of mode 2. Properties of these have been previously described in experimental works by Davis & Acrivos (1967), Maxworthy (1980) and Stamp & Jacka (1995). Maxworthy (1980) also investigated the generation of trains of solitary waves in a stratified fluid. We shall compare our results with those of previous investigations. We note, however, that detailed measurements of the velocity field induced by the waves have not previously been reported. Further, we obtain results that are not discussed in other work. In contrast to the study by Maxworthy,

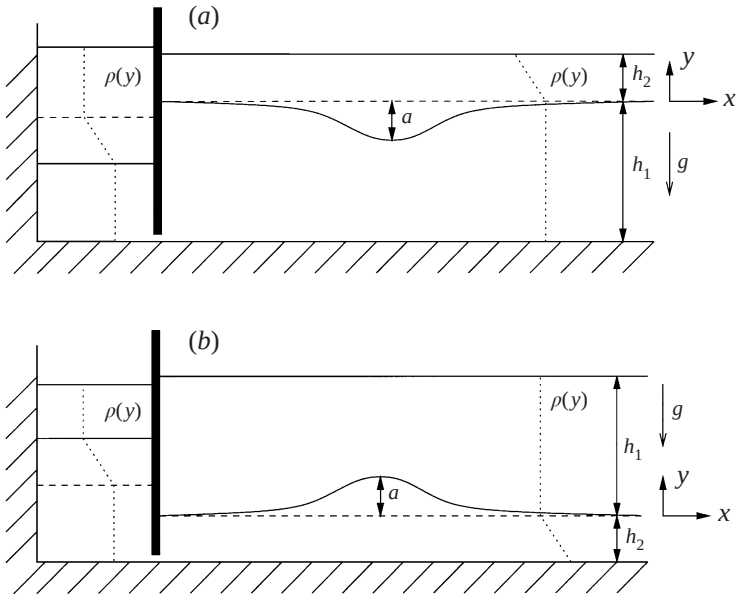

FIGURE 2. Sketch of the experiments. (*a*) Waves of depression propagate in a thin layer of linearly stratified fluid overlying a thick layer of homogeneous fluid. (*b*) Waves of elevation propagate in a thin layer of linearly stratified fluid lying under a thick layer of homogeneous fluid.

we focus here on the generation of a single solitary wave in the experiments. This is achieved by a careful adjustment of a trapped volume of fluid in the wave tank (see also Grue *et al.* 1999, for experiments with a two-layer fluid model with homogeneous layers). Fundamental differences between our experiments and e.g. those by Stamp & Jacka, include the length scale, which in this study is 50 times that of Stamp & Jacka. The value of the Reynolds number in this study covers the range of about 10^4–3×10^4 whereas Stamp & Jacka have a range of about 36–70.

The paper is organized as follows: § 2 describes the experimental arrangement and the PTV and PIV techniques. Section 3 describes the theoretical two-layer model, the integral equation method and the numerical procedure. In § 4 examples of the generated waves and results for the propagation speed of the waves are given. Results for waves with small amplitude are given in § 5. Detailed results for incipient breaking, in terms of velocity and vorticity plots, are given in § 6. The wave amplitude is then moderate. In § 7 breaking waves with large amplitude and broadening of the waves are discussed. In § 8 supplementary theoretical results are given, while § 9 contains concluding remarks.

2. Experiments

2.1. *Calibration of the two-layer model*

The experiments were carried out in a wave tank in the Hydrodynamics Laboratory at the University of Oslo. The wave tank is 25 m long and 0.5 m wide. We found it convenient to perform experiments in sections of the wave tank that were either 12.3 m or 18.4 m long. Most of the experiments are performed with a two-layer fluid where a lower homogeneous layer of brine has density $\rho_0 = 1.022\ldots\,\mathrm{g\,cm^{-3}}$ and depth h_1. A layer of fluid with depth h_2 and linear stratification is very gently filled on top of the lower layer. The density of the upper layer varies from $\rho_0 = 1.022\ldots\,\mathrm{g\,cm^{-3}}$

at the bottom, to ρ_1 at the top. ρ_1 is in the interval $0.999\ldots\,\mathrm{g\,cm^{-3}}$ to $1.004\ldots\,\mathrm{g\,cm^{-3}}$. We use floats with sponges to calibrate the upper layer. The time period of the filling can be several hours. The density profiles are recorded by a Yokogawa SC12 meter which determines the density from the local conductivity of the fluid. Complementary density measurements are obtained by a Mettler-Toledo DA-300M density meter which determines the density from the weight of the water with an accuracy of five significant digits. The values of ρ_0 and ρ_1 may vary somewhat from run to run due to practical reasons. Such variations are, however, unimportant to the results when the linear long-wave speed, c_0, is used as reference speed. It is in all cases determined theoretically by equation (3.20).

We also perform some experiments with the two-layer model upside down, i.e. with a thin linearly stratified fluid underlying a thick layer of (homogeneous) fresh water.

2.2. *Wave generation*

Waves are generated by trapping a volume of light or heavy fluid behind a gate which is lowered into one end of the tank. In the experiments with a thin linearly stratified fluid overlying a deep homogeneous fluid we gently add a volume of fresh water of density $0.999\ldots\,\mathrm{g\,cm^{-3}}$ behind the gate. A corresponding mass of the lower fluid then slowly moves to the other side of the gate such that hydrostatic balance is maintained. The depths of the layers in the main part of the tank are $h_1 = 62\,\mathrm{cm}$ and $h_2 = 15\,\mathrm{cm}$ while the trapped volume of fresh water behind the gate is varied. The position of the gate is in most cases at 0.5 m from the endwall of the tank. Exceptions are given in table 1 in § 7. By removing the gate a solitary depression wave is generated, propagating along the wave tank (figure 2*a*). In the cases with the two-layer model upside down we remove a certain volume of fresh water behind the gate in order to generate solitary waves of elevation (figure 2*b*). In a few of these experiments the trapped fluid behind the gate is stirred prior to the experiment.

By a careful adjustment of the position of the gate and depth of the trapped fluid we are in most of the cases able to generate a single solitary wave.

2.3. *Particle tracking and particle image velocimetry*

Particle tracking velocimetry (PTV) and particle image velocimetry (PIV) are powerful experimental techniques to quantify the velocities and the underlying dynamics of the waves observed in the wave tank. We shall use both methods here. In the PTV method individual particles are traced in sequences of images. This method is ideal when the local fluid acceleration is relatively small which occurs when the wave amplitude is small or moderate. In the PIV method the spatial cross-correlation between the position of groups of particles at two subsequent timeinstants is evaluated to estimate the local fluid velocity. We analyse the motion due to the moderate waves using both PTV and PIV. For the larger waves, introducing rather rapid fluid motion and strong variations of the vorticity, we find that PIV is required for precise measurements of the fluid motion.

Recordings are made in vertical sections of the wave tank by three monochrome COHU 4912 CCD cameras with a resolution of 575×560 pixels. The cameras are placed at positions 6.95 m, 10.63 m and 15.31 m from the wall at the upper end of the tank where the wave begins. A light sheet with thickness 5 cm at a distance of 10 cm from the glass wall of the tank is created in each section. The light sheets are vertical and parallel to the side of the tank. Powerful overhead projectors are used as light sources. The illuminated sections are seeded with particles of pliolite VTAC

with diameter in the range of 0.8–1 mm. The particles are treated in wetting agent for some time to obtain an effective neutral bouyancy for the range of the density profile.

The recording section seen by each camera is 50 cm long and 40 cm high. This means that a particle at rest normally is covered by four pixels in the CCD-chip in the camera. Each cell in the CCD-chip is charged for $1/50$ s. The transmission of the even and odd lines of the CCD-chip is sequential, however, giving an effective exposure time of $3/100$ s. In the experiments with small to moderate wave amplitude we observe a maximal velocity up to about $10\,\mathrm{cm\,s^{-1}}$, giving as a result exposures of the particles covering up to about eight pixels. For the largest waves, velocities up to about $20\,\mathrm{cm\,s^{-1}}$ are introduced in the fluid. In these runs we use a mechanical shutter in front of the cameras in order to enhance the accuracy. The effective exposure time then becomes $1/100$ s. The time between each frame is $1/25$ s.

The video recordings are digitized by a frame grabber card for subsequent analysis. Typically we identify 1200–4000 particles in each frame. In the PTV method we trace particles during five frames using the DigImage program developed and described by Dalziel (1992).

For PIV analysis we have implemented the method outlined by Willert & Gharib (1991). In addition, we employ interrogation window shifting as proposed by Westerweel, Dabiri & Gharib (1997). The images are interrogated in three steps where the first two steps are used to estimate the window shift with integer accuracy. In the final step the displacement is estimated to sub-pixel accuracy using a three-point Gaussian peak fit. Images are interrogated using interrogation windows of 32×32 pixels. In a few experiments we have also used 64×64 pixels due to insufficient particle seeding. The final velocity vectors are validated using a signal-to-noise ratio filter, where the signal-to-noise ratio is determined by the highest peak in the correlation plane divided by the second highest peak. For intermediate waves we normally require that this ratio is larger than 1.3, while for the large waves we use a value of 1.05. This less stringent value has to be applied mainly due to the turbulent character of a kernel of the large waves, with an accompanying increase of noise and decrease of peak height in the correlation plane. Vectors not satisfying this threshold are rejected and replaced by the mean of the surrounding vectors. Finally we apply a local median filter that effectively removes vectors that are significantly different from their neighbours. The PIV-algorithm may be found in Sveen (1998).

2.4. *Experimental accuracy*

The accuracy of the PTV method applied to internal wave experiments in a two-layer fluid, with a constant density in each layer, was analysed by Grue *et al.* (1999, §§ 2.3 and 7). That investigation includes further details of the PTV method used here. It was found that the error in the measured velocities relative to the linear long wave speed was less than about 7–8% in all cases. This analysis is also valid for the present experiments. Comparison between the PTV and PIV measurements shows that the accuracy of the two methods is approximately the same for the present experiments.

3. Theory

3.1. *Two-layer model*

As noted in the Introduction, we develop a theoretical model in parallel with the experiments. The basic equations of the fully nonlinear model are derived along the lines of previous studies (Long 1958; Yih 1960; Tung *et al.* 1982; Turkington *et al.*

1991). Recently, a fully nonlinear study of solitary waves of permanent form propagating in a stratified fluid has been done by Brown & Christie (1998). Coordinates O, xy are introduced, with the x-axis horizontal and the y-axis vertical, and with corresponding unit vectors $\boldsymbol{i}$ and $\boldsymbol{j}$. We consider motion in two dimensions where waves of permanent form are propagating with speed c horizontally in the fluid. Viewing the problem in a frame of reference which follows the waves, the motion becomes steady, with a horizontal current with speed c along the negative x-axis in the far field. The undisturbed fluid has a vertical density profile $\rho(y)$. We assume that the fluid is incompressible and inviscid. The former means that $\nabla \cdot \boldsymbol{v} = 0$ where $\boldsymbol{v} = (u, v)$ denotes the fluid velocity. Conservation of mass, $\nabla \cdot (\rho \boldsymbol{v}) = 0$, then gives that $\boldsymbol{v} \cdot \nabla \rho = 0$. Following the procedure of Yih (1960) we introduce pseudo-velocities $u' = (\rho/\rho_0)^{1/2} u$, $v' = (\rho/\rho_0)^{1/2} v$, where ρ_0 is a reference density. Furthermore we introduce a pseudo-stream function Ψ' such that $\boldsymbol{v}' = \nabla \Psi' \times \boldsymbol{k}$ where $\boldsymbol{k} = \boldsymbol{i} \times \boldsymbol{j}$. It follows that $\rho = \rho(\Psi')$. From the equations of motion the following relation may be derived (Yih 1960):

$$\rho_0 \nabla^2 \Psi' + g y \frac{\mathrm{d}\rho}{\mathrm{d}\Psi'} = \frac{\mathrm{d}H(\Psi')}{\mathrm{d}\Psi'} = h(\Psi'), \tag{3.1}$$

where $-\nabla^2 \Psi'$ determines the pseudo-vorticity and $H = p + \frac{1}{2}\rho(u^2 + v^2) + \rho g y$ is the Bernoulli constant, which is conserved along a streamline determined by $\Psi' =$ constant. Furthermore, p denotes pressure and g the acceleration due to gravity. $\mathrm{d}H/\mathrm{d}\Psi'$ is determined in the far field, giving

$$\frac{\mathrm{d}H}{\mathrm{d}\Psi'} = \left(\frac{\mathrm{d}p}{\mathrm{d}y} + \rho g \right) \frac{\mathrm{d}y}{\mathrm{d}\Psi'} + \frac{c^2}{2} \frac{\mathrm{d}\rho}{\mathrm{d}\Psi'} + g y \frac{\mathrm{d}\rho}{\mathrm{d}\Psi'}, \tag{3.2}$$

where c denotes the (constant) current speed in the far field. (c denotes, in the laboratory frame of reference, the (constant) wave speed, and is defined in the text prior to (3.1)). The vertical component of the equation of motion becomes in the far field $p_y + \rho g = 0$, which means that the first term on the right of (3.2) is zero. The pseudo-stream function is then decomposed into $\Psi' = \Psi'_\infty + \psi'$, where Ψ'_∞ satisfies

$$\frac{\mathrm{d}\Psi'_\infty}{\mathrm{d}y} = -c \left(\frac{\rho}{\rho_0} \right)^{1/2} \tag{3.3}$$

giving

$$\nabla^2 \Psi'_\infty = \frac{c^2}{2\rho_0} \frac{\mathrm{d}\rho}{\mathrm{d}\Psi'}. \tag{3.4}$$

Since $\mathrm{d}\rho/\mathrm{d}\Psi'$ is constant along each streamline, (3.1) becomes

$$\rho_0 \nabla^2 \psi' + g(y - y_\infty) \frac{\mathrm{d}\rho}{\mathrm{d}\Psi'} = 0, \tag{3.5}$$

where y and y_∞ are vertical coordinates on the same streamline, with y_∞ in the far field.

From now on we apply the Boussinesq approximation, i.e. exploit that $\Delta\rho/\rho$ is small. Integrating (3.3) we find $\Psi'_\infty = -cy[1 + O(\Delta\rho/\rho)]$, giving

$$y - y_\infty = \psi'/c\,. \tag{3.6}$$

Furthermore we have

$$\frac{g}{\rho_0} \frac{\mathrm{d}\rho}{\mathrm{d}\Psi'} = \frac{g}{\rho_0} \frac{\mathrm{d}\rho}{\mathrm{d}y} \frac{\mathrm{d}y}{\mathrm{d}\Psi'} \simeq \frac{N^2}{c} [1 + O(\Delta\rho/\rho)], \tag{3.7}$$

where $N^2 = -(g/\rho_0)(\mathrm{d}\rho/\mathrm{d}y)$ is the Brunt–Väisälä frequency. Within the Boussinesq approximation we may also replace the pseudo-stream function by the stream function Ψ such that $\boldsymbol{v} = \nabla\Psi \times \boldsymbol{k}$. Correspondingly, Ψ'_∞ and ψ' are replaced by Ψ_∞ and ψ, respectively. The motion is thus governed by the Helmholtz equation, i.e.

$$\nabla^2\psi + \frac{N^2}{c^2}\psi = 0. \tag{3.8}$$

Corresponding to the experiments we consider a two-layer model where the undisturbed fluid has an upper layer with a linear density profile and a lower layer with constant density, i.e.

$$\rho(y) = \begin{cases} \rho_0 - \Delta\rho\, y/h_2 & \text{for} \quad 0 < y < h_2, \\ \rho_0 & \text{for} \quad -h_1 < y < 0. \end{cases} \tag{3.9}$$

The line $y = 0$ separates the two layers. The upper layer is in the interval $0 < y < h_2$ and the lower layer in the interval $-h_1 < y < 0$. The Brunt–Väisälä frequency becomes a constant in the upper layer, and is there $N_0^2 = (\Delta\rho\, g)/(\rho_0 h_2)$. In the lower layer the Brunt–Väisälä frequency becomes zero. Let $\psi = \psi_2$ in the upper layer and $\psi = \psi_1$ in the lower. Then ψ_2 satisfies the Helmholtz equation in the upper layer, i.e.

$$\nabla^2\psi_2 + \frac{N_0^2}{c^2}\psi_2 = 0\,. \tag{3.10}$$

ψ_1 satisfies the Laplace equation in the lower layer, i.e.

$$\nabla^2\psi_1 = 0\,. \tag{3.11}$$

The upper boundary of the upper layer is a free surface. With $\Delta\rho/\rho$ small this boundary may be approximated by a horizontal rigid lid. We assume that the bottom of the lower layer is horizontal at $y = -h_1$. Thus,

$$\psi_2 = 0 \quad \text{at} \quad y = h_2, \tag{3.12}$$

$$\psi_1 = 0 \quad \text{at} \quad y = -h_1. \tag{3.13}$$

The two layers are separated by the streamline with vertical coordinate η where $\eta \to 0$ for $x \to \pm\infty$. The kinematic boundary condition requires that the fluid velocity is continuous at the boundary between the layers, i.e. that

$$\nabla(\psi_1 - cy) = \nabla(\psi_2 - cy) \quad \text{at} \quad y = \eta. \tag{3.14}$$

This gives

$$\frac{\partial\psi_2}{\partial s} - c\frac{\partial\eta}{\partial s} = 0 \quad \text{at} \quad y = \eta, \tag{3.15}$$

$$\frac{\partial\psi_1}{\partial s} - c\frac{\partial\eta}{\partial s} = 0 \quad \text{at} \quad y = \eta, \tag{3.16}$$

$$\frac{\partial\psi_1}{\partial n} = \frac{\partial\psi_2}{\partial n} \quad \text{at} \quad y = \eta, \tag{3.17}$$

where s denotes the arc length along the streamline $y = \eta$ and n the normal, pointing out of the lower fluid layer.

The formulation is fully nonlinear, where the stream functions $\psi_{1,2}$, the stream line η and the wave speed c are to be determined.

We note that the model may be generalized to also include a jump in the density and the fluid velocity at the boundary between the fluids.

3.2. *The wave speed for long linear waves*

Linear waves with wavenumber ν and wave speed c_0 may propagate horizontally in the fluid. The stream function ψ_2 in the upper layer then satisfies (3.10), with c replaced by c_0, while ψ_1 satisfies (3.11). Looking for solutions of the form $\psi_{1,2}(x, y) = \hat{\psi}_{1,2}(y)\cos \nu x$ satisfying (3.13)–(3.13) and (3.15)–(3.16), the latter two at $y = 0$, we find in the long-wave limit

$$\psi_2 = ac_0 \frac{\sin(N_0(y - h_2)/c_0)}{\sin(N_0 h_2/c_0)} \cos \nu x\,, \tag{3.18}$$

$$\psi_1 = -ac_0(1 + y/h_1)\cos \nu x\,. \tag{3.19}$$

The wave speed is determined using (3.17), i.e. putting $\partial\psi_1/\partial y = \partial\psi_2/\partial y$ at $y = 0$. This gives

$$\frac{N_0 h_2}{c_0} \cot \frac{N_0 h_2}{c_0} + \frac{h_2}{h_1} = 0, \tag{3.20}$$

where c_0 is obtained for $N_0 h_2/c_0$ in the interval $(\pi/2, \pi)$. For $h_2/h_1 \to 0$ the speed becomes $c_0 = N_0 h_2/(\pi/2)$. In our experiments, with $h_2/h_1 = 15/62$, the linear long-wave speed is $c_0 = N_0 h_2/1.711\ldots$.

3.3. *Solution by integral equations*

We solve the nonlinear problem (3.10)–(3.17) by means of integral equations and introduce two Green functions G_1 and G_2. The first Green function is a pole at $(x, y) = (x', y')$ and satisfies the Laplace equation (3.11), i.e.

$$G_1(x, y, x', y') = \ln \frac{r}{r_1}\,. \tag{3.21}$$

The second Green function is a pole at $(x, y) = (x', y')$ and satisfies the Helmholtz equation (3.10), i.e.

$$G_2(x, y, x', y') = \frac{\pi}{2}[Y_0(Kr) - Y_0(Kr_2)]\,, \tag{3.22}$$

where Y_0 denotes the Bessel function of second kind of order zero and $K = N_0/c$. Furthermore,

$$r = [(x - x')^2 + (y - y')^2]^{1/2}, \tag{3.23}$$

$$r_1 = [(x - x')^2 + (y + y' + 2h_1)^2]^{1/2}, \tag{3.24}$$

$$r_2 = [(x - x')^2 + (y + y' - 2h_2)^2]^{1/2}. \tag{3.25}$$

We let the stream functions be determined by

$$\psi_1 = \int_I \sigma_1(s')G_1(x, y, x'(s'), y'(s'))\mathrm{d}s'\,, \tag{3.26}$$

$$\psi_2 = \int_I \sigma_2(s')G_2(x, y, x'(s'), y'(s'))\mathrm{d}s'\,, \tag{3.27}$$

where $\sigma_1(s)$ and $\sigma_2(s)$ denote as yet unknown distributions, I denotes the contour $y = \eta$ and s arc length. We then consider the tangential and normal derivatives of ψ_1 and ψ_2 at I, finding

$$\frac{\partial\psi_{1,2}}{\partial s} = \mathrm{PV} \int_I \sigma_{1,2}(s')\frac{\partial G_{1,2}}{\partial s}\mathrm{d}s'\,, \tag{3.28}$$

$$\frac{\partial \psi_1}{\partial n} = -\pi\sigma_1(s) + \int_I \sigma_1(s')\frac{\partial G_1}{\partial n}\mathrm{d}s', \tag{3.29}$$

$$\frac{\partial \psi_2}{\partial n} = \pi\sigma_2(s) + \int_I \sigma_2(s')\frac{\partial G_2}{\partial n}\mathrm{d}s', \tag{3.30}$$

where in (3.28) PV denotes principal value. The boundary conditions (3.15)–(3.17) then give

$$\mathrm{PV}\int_I \sigma_1(s')\frac{\partial G_1}{\partial s}\mathrm{d}s' - c\frac{\partial \eta}{\partial s} = 0, \tag{3.31}$$

$$\mathrm{PV}\int_I \sigma_2(s')\frac{\partial G_2}{\partial s}\mathrm{d}s' - c\frac{\partial \eta}{\partial s} = 0, \tag{3.32}$$

$$-\pi[\sigma_1(s) + \pi\sigma_2(s)] + \int_I \left(\sigma_1(s')\frac{\partial G_1}{\partial n} - \sigma_2(s')\frac{\partial G_2}{\partial n}\right)\mathrm{d}s' = 0. \tag{3.33}$$

Choosing h_2 as length scale and c_0 as velocity scale (and h_2/c_0 as time scale) we determine $N_0 h_2/c_0$ by (3.20). Then the non-dimensional quantities Kh_2, σ_1/c_0, σ_2/c_0, η/h_2 and c/c_0 depend on the parameters h_1/h_2 and η_{max}/h_2, and not on $\Delta\rho/\rho$. Thus, within the Boussinesq approximation, the actual value of $\Delta\rho/\rho$ enters the problem only through c_0.

3.4. *Numerical procedure*

We look for symmetric solutions with respect to $x = 0$ which means that $\psi_{1,2}$ may be expressed by

$$\psi_{1,2} = \int_0^\infty \sigma_{1,2}(s')[G_{1,2}(x, y, x'(s'), y'(s')) + G_{1,2}(x, y, -x'(s'), y'(s'))]\mathrm{d}s'. \tag{3.34}$$

To discretize the equations we introduce a ξ-variable as coordinate along I replacing the arc length s as integration parameter. The collocation points $\xi = 1, 2, 3, \ldots, N$ are equally distributed in s which means that $s_\xi = \Delta s$ where $s_\xi \equiv \mathrm{d}s/\mathrm{d}\xi$. Equation (3.34) then becomes

$$\psi_{1,2} = \int_1^N \sigma_{1,2}(s')[G_{1,2}(x, y, x'(\xi'), y'(\xi')) + G_{1,2}(x, y, -x'(s'), y'(s'))]\Delta s\,\mathrm{d}\xi'. \tag{3.35}$$

It is convenient to introduce the complex variable $z = x + \mathrm{i}y$ and the complex functions $g_1(z, z')$ and $g_2(z, z')$ by

$$g_1(z, z') = \Delta s\left(\frac{\partial}{\partial s} - \mathrm{i}\frac{\partial}{\partial n}\right)G_1(x, y, x', y') = \frac{z_\xi}{z - z'} - \frac{z_\xi}{z - z'^* + 2\mathrm{i}h_1}, \tag{3.36}$$

$$\begin{aligned} g_2(z, z') &= \Delta s\left(\frac{\partial}{\partial s} - \mathrm{i}\frac{\partial}{\partial n}\right)G_2(x, y, x', y') \\ &= \frac{\pi}{2}\left(-KrY_1(Kr)\frac{z_\xi}{z - z'} + Kr_2Y_1(Kr_2)\frac{z_\xi}{z - z'^* - 2\mathrm{i}h_2}\right). \end{aligned} \tag{3.37}$$

The integrals in (3.31)–(3.33) and (3.35) are evaluated by using the trapezoid rule, except in the vicinity of the poles, where we adopt the procedure described by Dold & Peregrine (1985). Expanding the integrands in the vicinity of the poles in powers

of $(\xi - \xi')$ we arrive at the following discretized equations:

$$\sum_{\xi=1}^{N} \mathscr{A}_k(\xi, \xi')\sigma_k(\xi') - \sigma_{k,\xi}(\xi) = c\eta_{,\xi}(\xi)/\Delta s, \quad k = 1, 2, \tag{3.38}$$

$$-\pi(\sigma_1 + \sigma_2) + \sum_{\xi=1}^{N} \left[\mathscr{B}_1(\xi, \xi')\sigma_1(\xi') - \mathscr{B}_2(\xi, \xi')\sigma_2(\xi')\right] = 0, \tag{3.39}$$

where the matrices $\mathscr{A}_k(\xi, \xi')$ and $\mathscr{B}_k(\xi, \xi')$ read

$$\mathscr{A}_1(\xi, \xi') - \mathrm{i}\mathscr{B}_1(\xi, \xi') = \begin{cases} g_1(z, z') + g_1(z, -z'^*), & \xi' > 1,\ \xi' \neq \xi \\ g_1(z, z'), & \xi' = 1,\ \xi' \neq \xi \\ \dfrac{z_{\xi\xi}}{2z_\xi} - \dfrac{z_\xi}{z - z^* + 2\mathrm{i}h_1} + g_1(z, -z^*), & \xi' > 1,\ \xi' = \xi \\ \dfrac{z_{\xi\xi}}{2z_\xi} - \dfrac{z_\xi}{z - z^* + 2\mathrm{i}h_1}, & \xi' = \xi = 1; \end{cases} \tag{3.40}$$

$$\mathscr{A}_2(\xi, \xi') - \mathrm{i}\mathscr{B}_2(\xi, \xi') = \begin{cases} g_2(z, z') + g_2(z, -z'^*), & \xi' > 1,\ \xi' \neq \xi \\ g_2(z, z'), & \xi' = 1,\ \xi' \neq \xi \\ \dfrac{z_{\xi\xi}}{2z_\xi} + \dfrac{\pi}{2} K r_2 Y_1(K r_2) \dfrac{z_\xi}{z - z^* - 2\mathrm{i}h_2} + g_2(z, -z^*), & \xi' > 1,\ \xi' = \xi \\ \dfrac{z_{\xi\xi}}{2z_\xi} + \dfrac{\pi}{2} K r_2 Y_1(K r_2) \dfrac{z_\xi}{z - z^* - 2\mathrm{i}h_2}, & \xi' = \xi = 1, \end{cases} \tag{3.41}$$

and an asterisk denotes complex conjungate.

The equations are solved by considering c/c_0, $\eta(1)/h_2$, $\sigma_1(1)/c_0$, $\sigma_2(1)/c_0$, $x(\xi)_\xi/h_2$, $\eta(\xi)_\xi/h_2$, $\sigma_1(\xi)_\xi/c_0$ and $\sigma_2(\xi)_\xi/c_0$ for $\xi = 2, \ldots, N$, as unknowns. Furthermore, we require that $\eta(N) = 0$ and that $\sigma_1(s)$ and $\sigma_2(s)$ are smooth at the truncation of I, i.e. $\sigma_{1,\xi}(N-1) = \sigma_{1,\xi}(N)$ and $\sigma_{2,\xi}(N-1) = \sigma_{2,\xi}(N)$. The system is solved by applying a variant of the Newton–Raphson method for a prescribed amplitude a/h_2, i.e. $\eta(1)/h_2 = -a/h_2$. At each iterative step, $x(\xi)/h_2$, $\eta(\xi)/h_2$, $\sigma_1(\xi)/c_0$ and $\sigma_2(\xi)/c_0$ are obtained from their respective derivatives by the four-point Lagrangian integration formula, i.e.

$$\int_{\xi-1}^{\xi} f(\zeta)\mathrm{d}\zeta = \tfrac{1}{24}\left[-f(\xi+1) + 13f(\xi) + 13f(\xi-1) - f(\xi-2)\right]. \tag{3.42}$$

The second derivative $z_{\xi\xi}$ is found by using the four-point Lagrangian difference formula.

The differentiations for obtaining the Jacobi matrix in the secant method are usually approximated using first-order discrete differences, with the matrices $\mathscr{A}_k$ and $\mathscr{B}_k$ considered as constants during the differentiations. This procedure increases the number of iterations somewhat compared to using the full Jacobi matrix, but leads to a relatively faster scheme.

Particular care is needed when the value of $Kh_2 = N_0 h_2/c$ is close to $\pi/2$, where a full Jacobi matrix is needed in the computations.

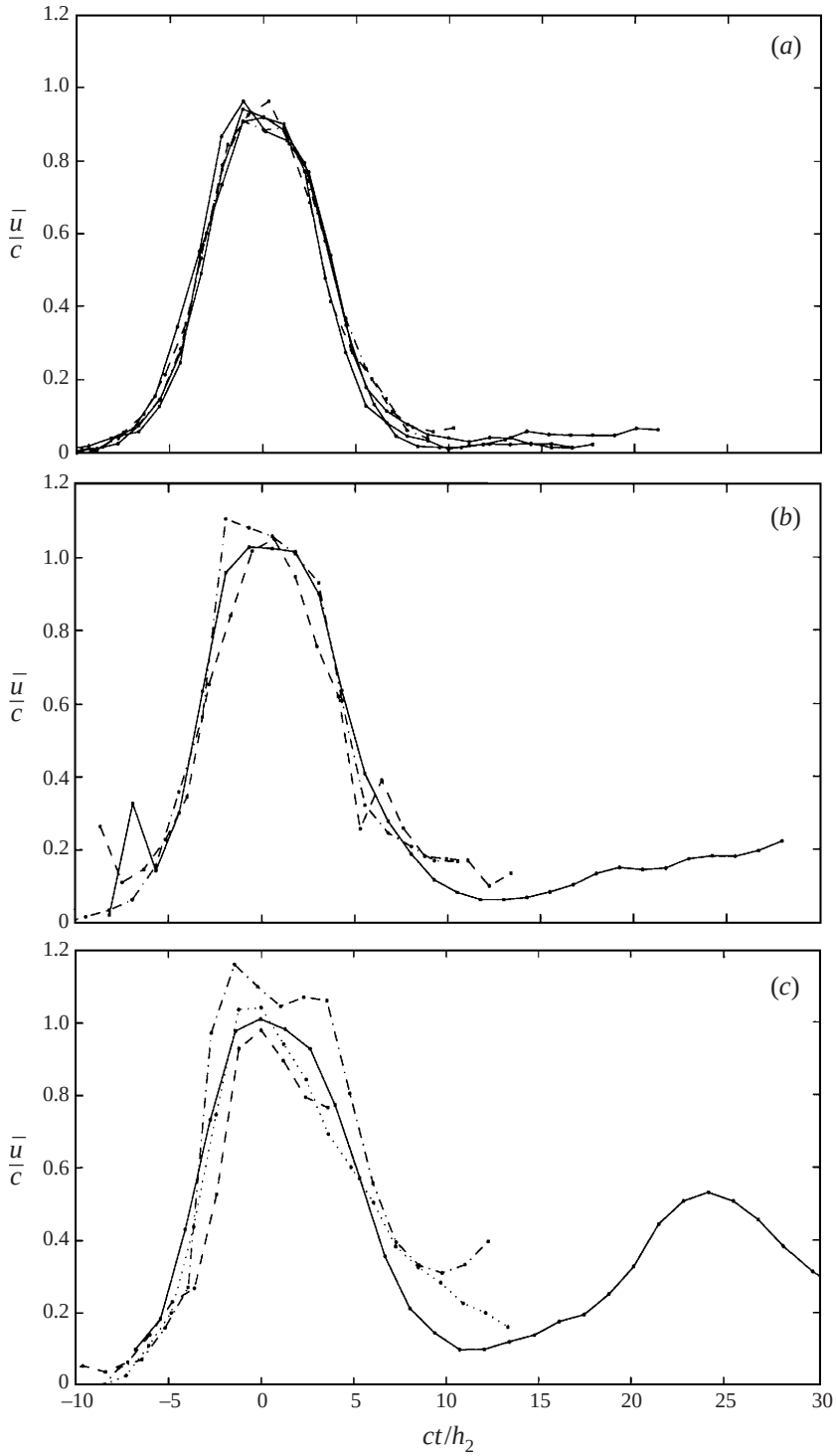

FIGURE 3. For caption see facing page.

4. Propagation of solitary waves

4.1. *Examples of generated waves*

Internal solitary waves of depression or elevation are generated as described in §§ 2.1–2.2. The fluid motion is locally rather violent at the position of the gate when it is opened. After a while, however, the initial disturbance develops into a solitary wave propagating along the tank, and the initially violent motion disappears. At the end of the tank the wave is reflected. The solitary wave travels back and forth for quite a long time before the motion fades out.

The fluid velocities are recorded when the wave travels past the camera positions at 6.95 m (camera 1), 10.63 m (camera 2), 15.31 m (camera 3), and when the wave returns. Time histories of a vertically averaged horizontal velocity $\bar{u}$ close to the free surface are shown in figure 3 for the experiment sketched in figure 2(*a*). The velocity $\bar{u}$ is defined in equation (7.1) in § 7.3 and in this figure is normalized by the wave speed c, measured as described in § 4.2. The horizontal velocity close to the bottom of the wave tank is also obtained for the inverted two-layer model, sketched in figure 2(*b*). In some of these measurements the trapped volume behind the gate is stirred prior to the runs to investigate how sensitive the generated waves are to the initial conditions.

The various experiments with the thin upper layer over a thick layer and with this inverted give approximately the same time histories of the normalized horizontal fluid velocity, when the initial volume is the same. This result is found from a large set of experiments. An example is provided in figure 3 for an initial volume of 100 dm^3 (depth 0.4 m $\times$ length 0.5 m $\times$ tank-width 0.5 m). The horizontal velocity is obtained at cameras 2 and 3 for both two-layer models. In another example the velocity profiles at the maximal depression or elevation of the wave are shown for an initial volume of 50 l (depth 0.2 m $\times$ length 0.5 m $\times$ tank-width 0.5 m), see figure 9(*b*). Several other runs and comparisons are also made, giving the same result, but are not shown.

Another aspect of interest is how the wave properties are maintained during the propagation. This is shown in figures 3(*b*) and 3(*c*) for initial volumes of 150 l and 200 l (runs B and C in table 1, § 7.3). Recordings of the horizontal velocity made at cameras 2 and 3, and for the reflected wave at cameras 3 and 2, show that the wave properties are maintained, apart from a small continuous decay of the wave amplitude and wave speed. The recordings in figures 3 and 9(*b*) illustrate the robustness of the wave generation procedure.

The release of trapped fluid may easily generate a train of solitary waves, see e.g. Maxworthy (1980). This is true also in a few cases in our set of experiments. An example is shown in figure 3(*c*) for one of the largest leading waves. By a careful adjustment of the position of the gate and the depth of the trapped fluid, however, we are in most cases able to generate a single solitary wave.

The motion far away from the gate quite rapidly becomes approximately symmetric with respect to the centre of the wave. This is true at the position of the first camera

---

FIGURE 3. Time histories of $\bar{u}$ as defined in (7.1) close to the free surface. (*a*) Initial volume 100 dm^3. The three solid lines measurements at camera 3: ordinary models show: (figure 2*a*) and inverted model (figure 2*b*) with and without stirred trapped fluid behind the gate. Dash dotted line: measurements at camera 2, experiment as in figure 2(*b*). Dashed line: measurements at camera 2, experiment as in figure 2(*b*), with stirred trapped fluid behind the gate. (*b*) 150 l. Experiment as in figure 2(*a*). Dash dotted line: camera 2. Solid line: camera 3. Dashed line: camera 2, reflected wave. (*c*) As (*b*), but 200 l initial volume (run C in table 1). Also, dotted line: camera 3, reflected wave.

when the wave amplitude is small or moderate (figure 6 and results not shown). Further down the tank the moderately large waves break, as described in § 6.1. For disturbances with large amplitude, a distinct wave motion takes place at the position of cameras 2 and 3 (figure 3).

During the initial phase of the individual runs the fluid motion may resemble a gravity current. The dynamics of the head of a gravity current was investigated by e.g. Simpson & Britter (1979, see particularly figure 5), finding that this head moves with a speed of approximately $1.2 \times (g'\tilde{h})^{1/2}$, where g' denotes the reduced gravity and $\tilde{h}$ the thickness of the tail of the gravity current. The thickness $\tilde{h}$ undergoes a monotonic decay with time and rapidly becomes very small compared to the depth h_2 of the layer with linear stratification.

The volume of the tail of a gravity current in the experiment may be estimated from the initially trapped volume minus the reduced volume of the homogeneous layer due to the generated wave. The latter may be estimated by the wave amplitude times the tankwidth times the wavelength, λ. Here, λ is defined in (7.2) and results are given in figure 21. The relative difference between the initially trapped volume and the estimated volume of the wave, at camera 1 for the small to moderate waves (figure 5), and at cameras 2 and 3 for the large waves (figure 3), is found to be small (less than 0.1 in all cases). We estimate that $\tilde{h}/h_2 < 0.01$ for the cases in figures 5 and 3. The observed wave speed in the present experiments is much larger than the estimated speed of a gravity current.

4.2. *Propagation speed*

The waves have quite distinct properties, among others a clearly defined propagation speed c. We measure the speed of the wave by first identifying a vertical line through approximately the centre of the wave which is characterized by a vanishing vertical fluid velocity. This line corresponds to the symmetry line of the theoretical model (see (3.34) with $x = 0$). More specifically we proceed as follows:

(a) The experimental velocity matrix is obtained in the coordinates (x_m, y_n), $m = 1,\ldots,M$, $n = 1,\ldots,N$. In a frame capturing the centre of the wave, we search the velocity matrix for the intervals $(x_{\tilde{m}}, x_{\tilde{m}+1})_n$, $\tilde{m} = 1,\ldots,\tilde{M}$, $(1 \leqslant \tilde{M})$, $n = 1,\ldots,N$, where the vertical component of the velocity changes sign.

(b) The position of the vertical line is determined by the median of the endpoints of the intervals with smallest vertical velocity.

The speed is estimated by the travel distance of this line between two cameras divided by the elapsed time. The method is carefully checked and is found to be robust.

The waves in the experiments have no clearly defined amplitude. For example, from the measured fluid velocities we are unable to identify a sharp boundary between the upper stratified layer and the lower homogeneous layer. (Measurements of the actual density profile would perhaps resolve this problem.) The theoretical model may, however, be applied to define the amplitude of the wave since the boundary between the two layers there is sharp. We therefore define the amplitude of the experimental wave from the theoretical model by fitting the experimental and theoretical velocity fields. For the largest waves the experiments exhibit a region with strong breaking close to the free surface above the centre of the wave. In this case the experimental and theoretical velocity fields below the region with breaking are compared.

An alternative is to fit two straight lines to individual velocity profiles: one line to the velocity profile in the lower part of the upper layer and one line to the profile in the upper part of the lower layer. The amplitude of the wave is then defined by the

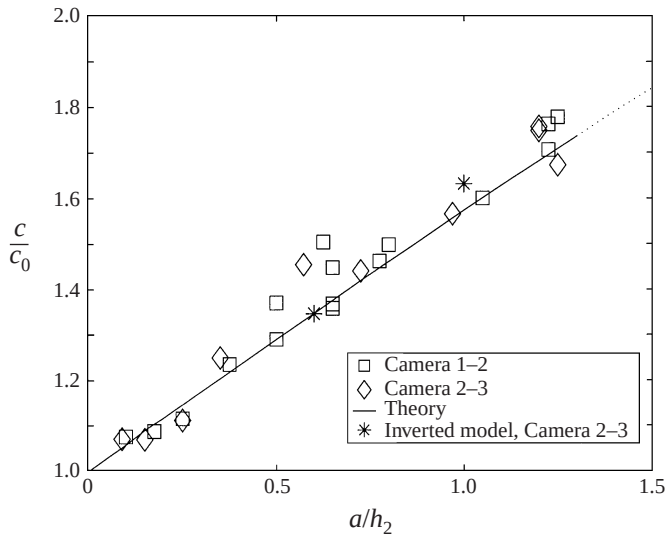

FIGURE 4. Propagation speed c vs. wave amplitude a. c_0 determined theoretically by (3.20). Cameras at positions 6.95 m, 10.63 m and 15.31 m from the wall at the upper end of the tank. Experiments as in figure 2(a, b). Thickness of stratified layer: $h_2 = 15$ cm. Thickness of homogeneous layer $h_1 = 62$ cm.

intersection between the two lines. This method gives approximately the same result as the one previously mentioned.

In figure 4 the measured and theoretical speed of the solitary waves is shown as a function of the wave amplitude. Generally, the agreement between experiment and model is good for all wave amplitudes. There is particularly good agreement for small wave amplitude. This is true not only for the propagation speed, but also for the entire velocity field induced by the wave. (Results for the latter are given in § 5.) This good agreement between the measured and computed c, for small a/h_2, illustrates, among other things, the usefulness of the method of extracting c in the experiments.

Experiments are performed with an increasing trapped volume behind the gate. Waves with a maximal speed and maximal amplitude are then encountered. The maximal observed propagation speed is about 1.78 times the linear long-wave speed, and the maximal amplitude is about 1.25 times the depth of the upper shallow layer (see also table 1). We note that the results exhibit a good correspondence between the measured and computed propagation speed even for these large waves. This is rather surprising, since the theory does not capture several effects observed in the experiments when the wave amplitude is large. The most visible difference is the rather dominant region with strong breaking taking place above the centre of the wave in the experiments. Furthermore the theoretical model does not predict the maximal values of the amplitude, the propagation speed and the fluid velocities observed in the experiments. The model predicts instead a continuous growth of the fluid velocity, wave amplitude and wave speed beyond the experimental maximal values. The model also predicts a region of recirculating fluid above the centre of the wave when the theoretical amplitude exceeds $a/h_2 = 0.855$. In this region the fluid velocity at the free surface becomes larger than the propagation speed. Examples are included in figure 22 in § 8. A theoretical fluid velocity which exceeds the wave speed indicates that breaking should occur for realistic waves. This is true, as the experiments show.

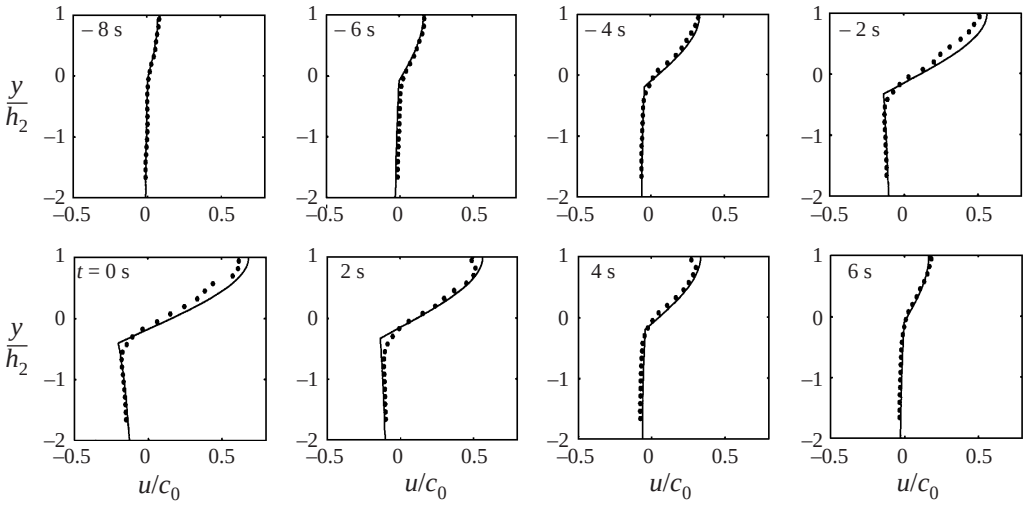

FIGURE 5. Time series at camera 1 of the horizontal velocity u vs. vertical coordinate y. Initial volume: 30 dm^3. PTV (dots) and theory with $a/h_2 = 0.4$ (solid line). $t = 0$ denotes the middle of the wave in this and subsequent similar figures.

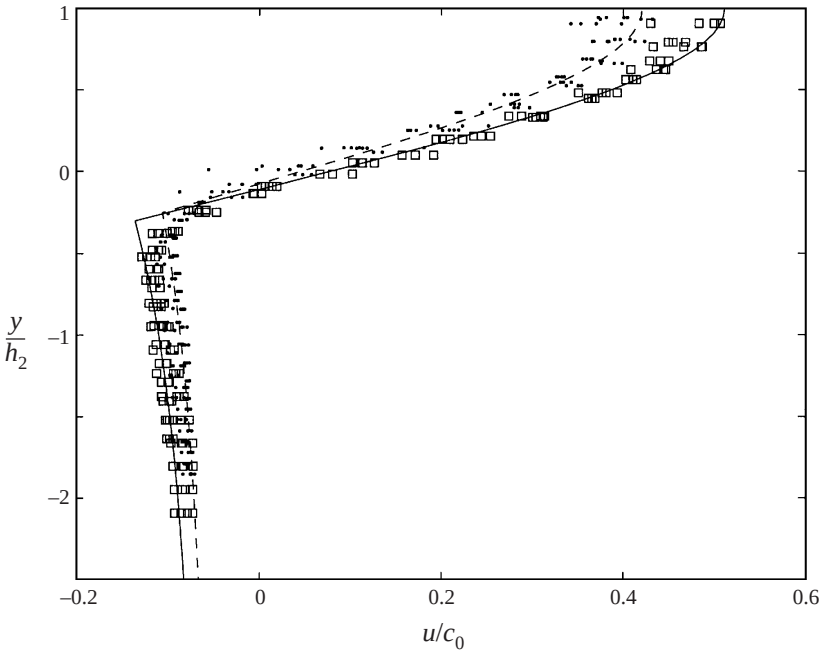

FIGURE 6. Velocity profile at the maximal depression of the wave. PTV: squares, camera 1; dots, camera 2. Initial volume: 20 dm^3. Theory with $a/h_2 = 0.3$ (solid line) and $a/h_2 = 0.25$ (dashed line).

The results in figure 4 show that the propagation speed is an approximately linear function of the amplitude, with $c/c_0 \simeq 1 + 0.57a/h_2$. So far results have been obtained for $h_1/h_2 = 4.13$. Computations of c/c_0 for other h_1/h_2 also exhibit an approximately linear relationship with the amplitude (figure 24). This means that weakly nonlinear theory, which is valid for small a/h_2, should predict a propagation speed that fits with

the measurements and the fully nonlinear theory even for amplitudes which are not small. A linear relationship between c and a has also been found in the experiments by Stamp & Jacka (1995), who investigated mode 2 solitary waves propagating in the pycnocline between two fluids of constant densities. They found $c/c_0 \simeq 1 + 0.49a/h_2$ and a good comparison between experiments and a fully nonlinear theory. Their stratification is different to ours, however. (Surprisingly, they note that a weakly nonlinear theory does not fit well with their measurements.)

The linear relationship between the wave speed and the wave amplitude illustrates that the dynamics of finite-amplitude waves in a stratified fluid has fundamental differences from the dynamics of finite-amplitude waves in a two-layer fluid with a constant density in each of the layers. In the latter case there is not a linear relationship between the wave speed and the wave amplitude, except when the wave amplitude is small. Documentation may be found in Grue *et al.* (1999, figure 6), comprising both experimental and theoretical results.

5. Properties of waves with small amplitude

Results for the velocity field induced by waves with small (finite) amplitude are next considered. The fluid velocities close to the free surface become comparable with the linear long-wave speed c_0 even for rather moderate wave amplitude. More specifically, the maximal horizontal velocity is about 65% of the linear wave speed c_0 for $a/h_2 = 0.4$ (figure 5). The smallest waves exhibit a decay of the amplitude during the propagation along the tank (figure 6). Such a decay is more pronounced for waves with small rather than large amplitude. We find good agreement between experiments and theory. This good agreement shows that the model provides a useful description of the solitary waves under consideration, for small (finite) amplitude.

For a closer comparison between experiment and theory, the vorticity field due to the wave is considered. The theoretical vorticity, ω, is obtained from (3.5)–(3.7) giving

$$\omega = -\nabla^2\psi = (y - y_\infty)\, N^2/c, \tag{5.1}$$

where y and y_∞ are on the same streamline. Thus, the local value of ω is determined by the vertical excursion of a streamline from its level far upstream times a constant, since the Brunt–Väisälä frequency is constant in the upper layer. In the lower layer the theoretical vorticity is zero, since N there is zero. The experimental vorticity $\partial v/\partial x - \partial u/\partial y$ is obtained from the PTV analysis using a standard difference method.

The vorticity at a given position in the tank is initially zero, becomes non-zero during the passage of the wave and reduces to zero when the wave has disappeared. There is a good correspondence between experiment and theory at the first camera position (figure 7). Further downstream, at the second camera, some differences between experiment and theory are noted in the leading part of the wave rather close to the free surface (figure 8). Such differences become more pronounced for waves of larger amplitude.

6. Waves with moderate amplitude

In the next experiments waves with larger amplitude are generated. Now the magnitude of the induced fluid velocity close to the free surface becomes comparable to the wave speed, but is still somewhat smaller. Examples of the velocity profile at the maximal depression of the wave are displayed in figure 9. It turns out that the maximal horizontal fluid velocity is approximately 70%, 80% and 85% of the wave

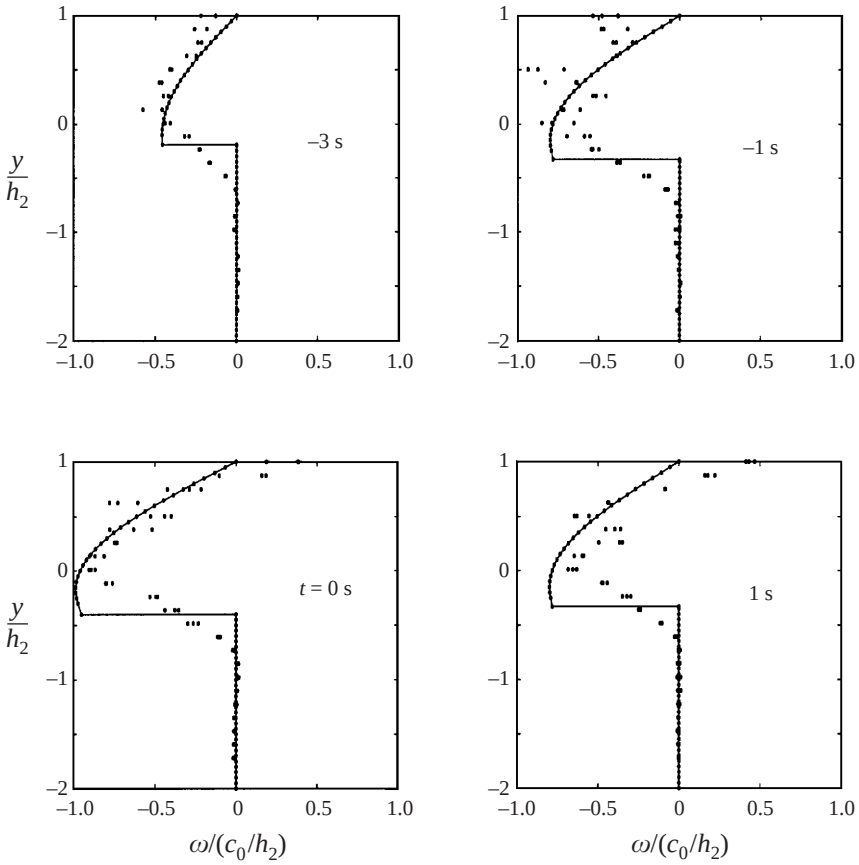

FIGURE 7. Time series at camera 1 of the vorticity $\omega = \partial v/\partial x - \partial u/\partial y$ vs. vertical coordinate y. Time increment 1 s between each picture. Initial volume: 30 dm^3. PTV (dots) and theory with $a/h_2 = 0.4$ (solid line).

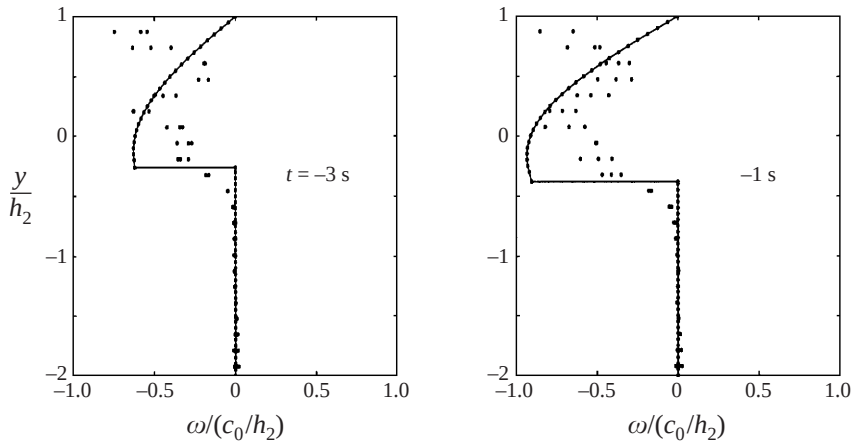

FIGURE 8. Same as figure 7, but at camera 2.

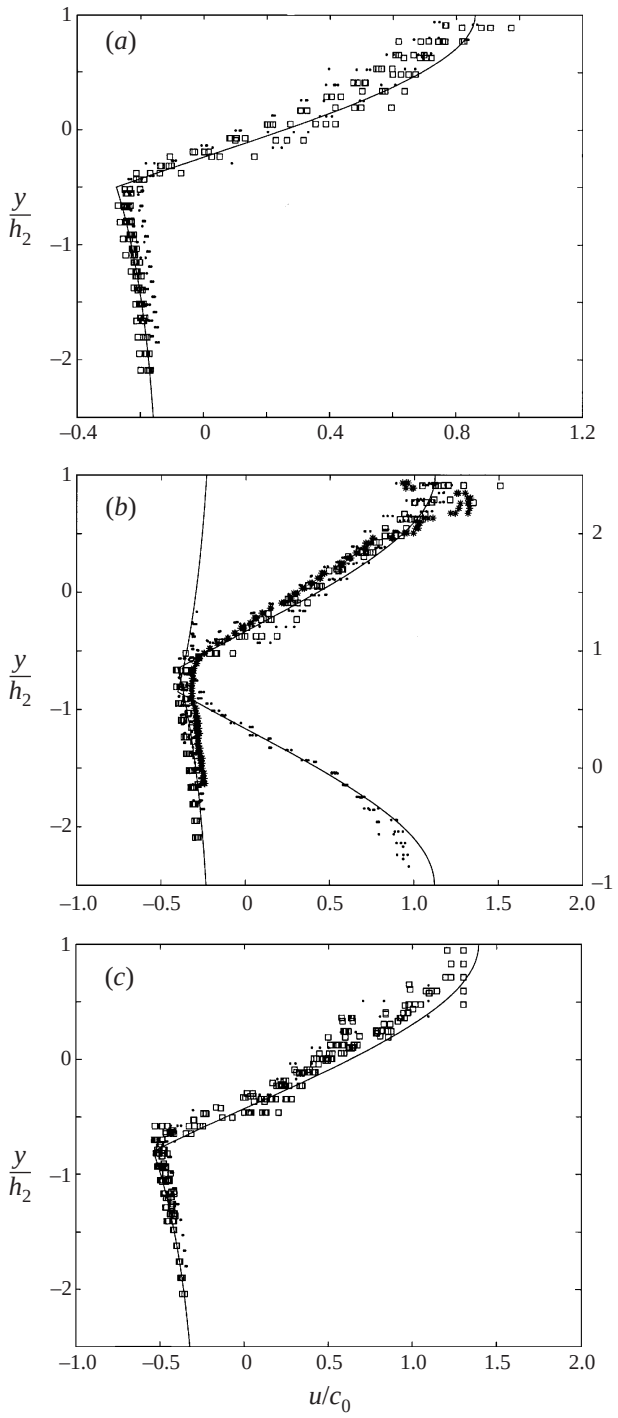

FIGURE 9. Same as figure 6, but (*a*) PTV, initial volume 40 l, theory with $a/h_2 = 0.5$ (solid line); (*b*) PTV and PIV, initial volume 50 l, stars: camera 3, theory with $a/h_2 = 0.65$ (solid line), inverted two-layer model (right-hand axis, dots) (see figure 2*b*); (*c*) PTV and PIV, initial volume 65 l and theory with $a/h_2 = 0.8$ (solid line). (Note the differences in scale.)

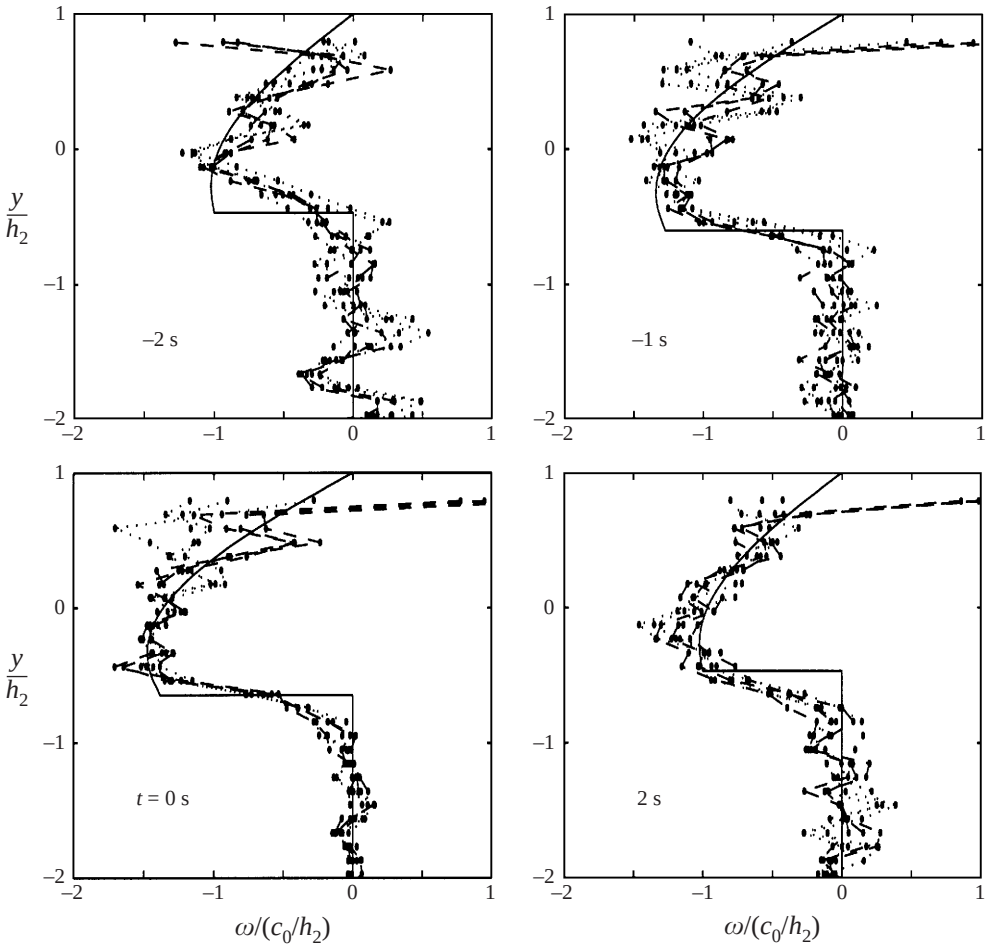

FIGURE 10. Time series of several neighbouring sets of PIV/PTV results at camera 1 of the vorticity $\omega = \partial v/\partial x - \partial u/\partial y$ vs. vertical coordinate y. Initial volume: 50 dm^3, PIV. Two different runs. Run 1: $\rho_0 = 1.0226\,\mathrm{g\,cm^{-3}}$, $\rho_1 = 0.9989\,\mathrm{g\,cm^{-3}}$, $c_0 = 11.38\,\mathrm{cm\ s^{-1}}$ (dash-dotted line). Run 2: $\rho_0 = 1.0225\,\mathrm{g\,cm^{-3}}$, $\rho_1 = 0.9991\,\mathrm{g\,cm^{-3}}$, $c_0 = 11.36\,\mathrm{cm\,s^{-1}}$) (dotted line). Theory (solid line). The black dots represent computational points.

speed in figures 9(*a*), 9(*b*) and 9(*c*), respectively. The results are obtained from several runs with recordings at all the three camera positions. The theoretical and measured velocity profiles compare rather well. The comparison is particularly good away from the free surface.

6.1. *Breaking*

As mentioned above, most of the experiments are performed with a thin stratified layer above a thick homogeneous layer. In these experiments, with waves of moderate amplitude, we observe that local breaking takes place in the leading part of the wave close to the free surface. The breaking is repeatable, and develops during the propagation of the wave. More specifically, no breaking is observed at the first camera position (at 6.95 m), but is, however, observed at the second camera (at 10.63 m). The breaking continues to develop and becomes stronger at the third camera position (at 15.31 m) than at the previous one. The wave hits the vertical wall at the end of the

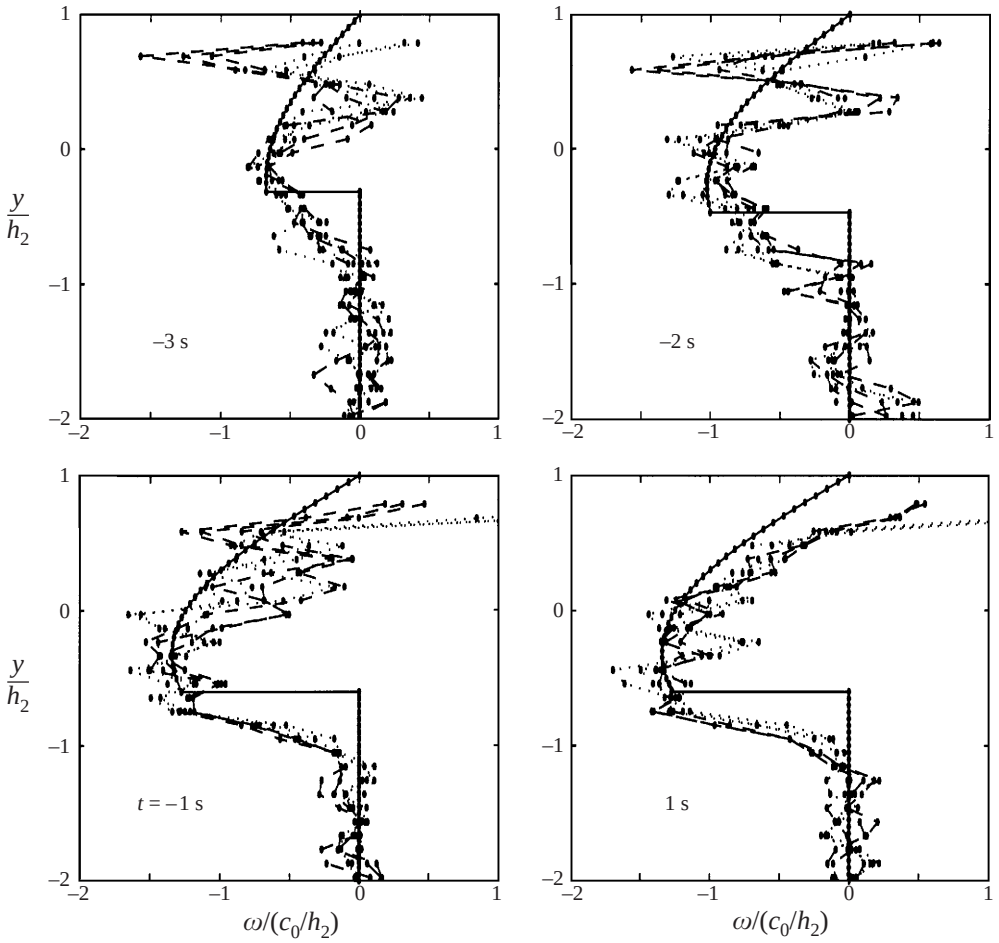

FIGURE 11. Same as figure 10, but camera 2.

tank, becomes reflected and rapidly recovers the form of a solitary wave propagating in the reverse direction. Now the breaking in the leading part of the wave has disappeared, however. No breaking is visible at the third camera (at 15.31 m) which is closest to the reflecting wall. In the middle of the tank, at camera two, breaking is clearly visible in the leading part of the reflected wave, on the other hand. The breaking continues to develop during the propagation and is stronger at camera one (at 6.95 m) than at camera two.

The breaking may be investigated more closely by examining the vorticity field. The theoretical vorticity is given by (5.1) and the experimental vorticity is evaluated from the PIV analysis by a least-squares operator, i.e. $(\mathrm{d}f/\mathrm{d}x)_{\mathrm{i}} = (2f_{i+2} + f_{i+1} - f_{i-1} - 2f_{i-2})/(10\Delta X)$. This operator is most suitable since it reduces the effect of random errors in the PIV method (Raffel, Willert & Kompenhans 1998, p. 159). At the first camera we find, apart from some small fluctuations of the experimental vorticity, a relatively good correspondence between theory and experiment, see figure 10. The results in figures 10–12 correspond to the velocity profile(s) in figure 9(*b*).

At the position of camera 2 the vorticity is different from that at camera 1. Now a rather pronounced breaking appears in the leading part of the wave, approximately in

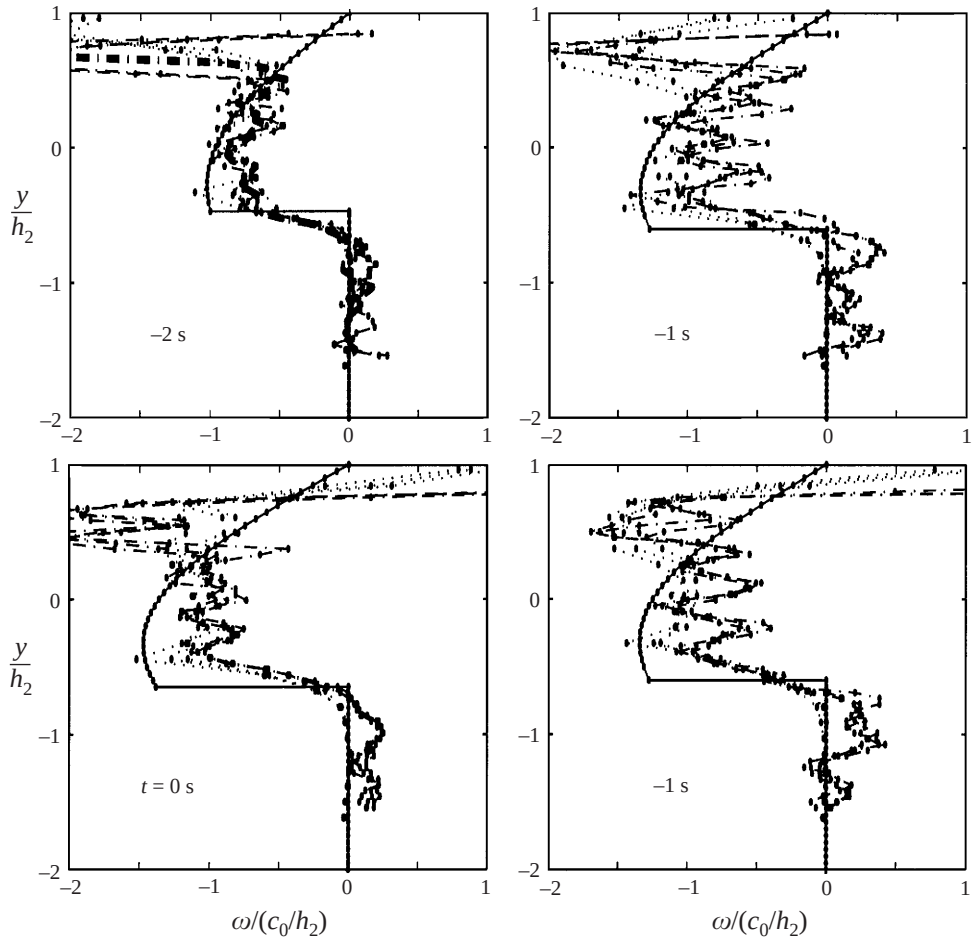

FIGURE 12. Same as figure 10, but camera 3, and a different run $\rho_0 = 1.0225\,\mathrm{g\,cm^{-3}}$ $\rho_1 = 1.0040\,\mathrm{g\,cm^{-3}}$ $c_0 = 9.01\,\mathrm{cm\ s^{-1}}$. PIV (dots with solid line), PTV (dots with dotted line), theory (solid line).

the middle of the stratified layer. This is shown in figure 11 by a pronounced negative vorticity in the fore part of the wave for $y/h_2 \approx 0.5$–0.7 and an almost vanishing vorticity for $y/h_2 \approx 0.2$–0.4. The breaking is observed in several different runs, and its appearance is always the same (figure 11). The breaking continues to develop during the propagation as shown by the recordings at camera 3 (figure 12).

The breaking may also be visualized more directly by decomposing the velocity field as $\boldsymbol{v} = \overline{\boldsymbol{v}} + \boldsymbol{v}'$, where $\overline{\boldsymbol{v}}$ denotes an averaged fluid velocity close to the free surface at the centre of the wave. The perturbation velocity field $\boldsymbol{v}'$ contains local vortices in the fore part and in the centre of the waves (figure 13). The vortices are not seen in a frame moving with the wave speed. Similar results (not shown here) are also obtained for smaller waves with amplitude $a/h_2 \simeq 0.5$ (figure 9*a*). The breaking is then somewhat less pronounced. We note that separate recordings of the fluid velocities at the free surface, taken from above, show that the motion is two-dimensional.

The experimental vorticity exhibits some oscillations along the vertical coordinate in addition to the pronounced vorticity in the leading part of the wave already described. The oscillations are present both in the upper and the lower fluid, where in the latter

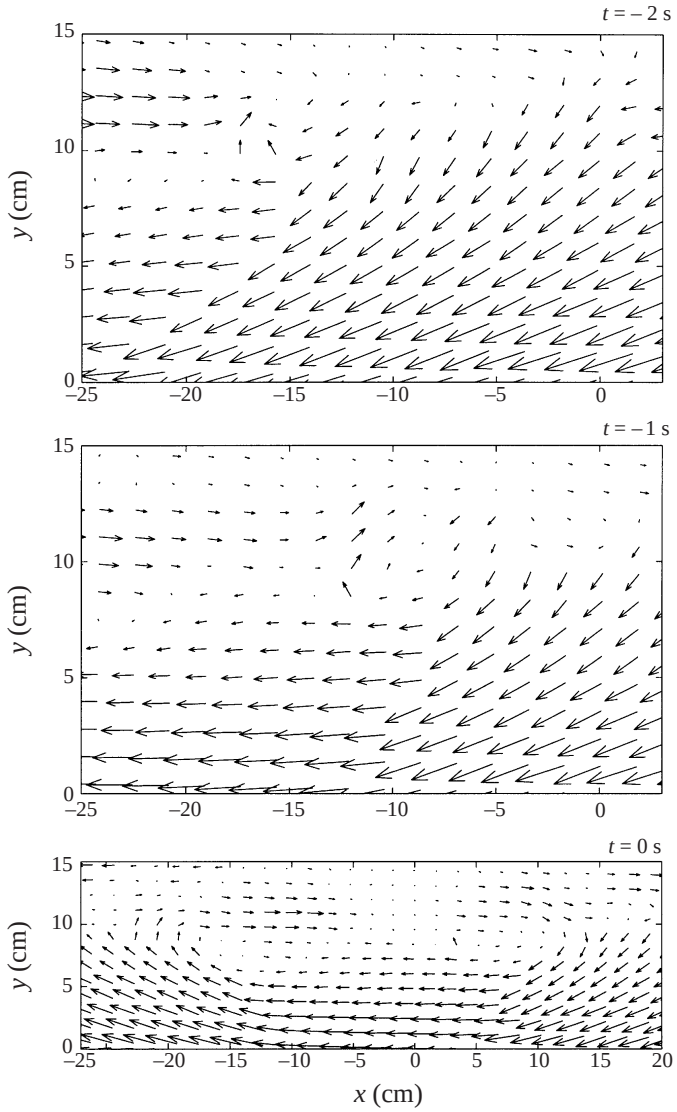

FIGURE 13. Velocity field $\boldsymbol{v}' = \boldsymbol{v} - \bar{\boldsymbol{v}}$, where $\bar{\boldsymbol{v}}$ is defined in the text. Initial volume 50 l. Camera 3. Close up of the region $0 < y < 15$ cm below the free surface (where the latter is at $y = 15$ cm). (For reference: the depth of the upper layer at rest is 15 cm.) $t = 0$ s denotes middle of the wave.

the density is constant, and the vorticity should be zero. We are uncertain about an explanation of the oscillations, but speculate that inaccuracies in the recording technique and shortcomings in the subsequent image processing are causes. A high-resolution PIV system would perhaps provide better evidence on this point. We note, however, that the amplitude of the oscillations of the vorticity is much less than the magnitude of the pronounced vorticity caused by the breaking in the fore part of the waves. Thus, the uncertainty in the vorticity is much smaller than the magnitude of the dominant phenomenon. We add that the theoretical vorticity provides a reference for the experimental vorticity. When breaking is not observed in the experiments, a relatively good correspondence between the theoretical and the experimental vorticity is found, except close to the free surface (figure 10).

The vorticity at the free surface extracted from PIV analysis is almost always rather large and positive (figures 10–12). Truncation effects may, however, distort the velocity and vorticity estimation close to the boundaries of the pictures. The experimental vorticity at or in the close vicinity of the free surface may therefore not be accurate.

6.2. *Non-breaking waves of moderate amplitude*

To check if the breaking is caused by shear instability, the Richardson number $Ri = N^2/(\partial u/\partial y)^2$ is evaluated. A sufficient condition for stability of a (stationary) stratified flow is that the Richardson number everywhere exceeds 1/4. The velocity gradient $\partial u/\partial y$ may be approximated by the vorticity ω. Taking N as constant in the upper layer, applying (5.1) and $c_0 = N_0 h_2/1.711\ldots$, see the text below (3.20), an estimate of the Richardson number is obtained:

$$Ri \simeq \left(\frac{c/N}{y - y_\infty}\right)^2 \simeq 0.34 \left(\frac{c/c_0}{(y - y_\infty)/h_2}\right)^2 > 0.34 \left(\frac{c/c_0}{a/h_2}\right)^2, \tag{6.1}$$

where y and y_∞ are on the same streamline of the wave. This gives $Ri > 1/4$ everywhere in the computed waves that are relevant to the experiments. Even for the maximal experimental ω in figures 11–12 the Richardson number significantly exceeds 1/4. We are then led to believe that the observed breaking is caused by another mechanism than shear instability.

Additional experiments are performed with the purpose of investigating the influence of the free-surface boundary conditions on the breaking just discussed. The first set of experiments is performed with the inverted model (figure 2*b*). The initial volume is varied stepwise from 50 dm^3 to 100 dm^3. Breaking of the waves is not seen until the induced fluid velocity becomes comparable to the wave speed. The initial volume is then 80 dm^3. The measured fluid velocities in the non-breaking waves show good correspondence with the theoretical model.

Another set of experiments is performed with the thin stratified layer above the thick homogeneous layer (figure 2*a*), but now the upper layer is capped by plates of polystyrene. This eliminates the effect of a thin elastic film at the free surface. The results of these experiments are the same as those with the inverted model: wave breaking is not observed until the fluid velocity is comparable to the wave speed.

From these and the previous experiments it is rather evident that the breaking described in § 6.1 depends on the boundary conditions at the free surface. We may speculate that the surface tension may be the cause. We note that the magnitude of the surface tension may vary from experiment to experiment. The breaking of the waves described in § 6.1 is nevertheless found to be repeatable for initial volumes larger than 50 dm^3 and wave amplitudes a/h_2 larger than about 0.65.

7. Waves with large amplitude

Several experiments with the two-layer model in figure 2(*a*) are performed by gradually increasing the initial volume above the levels already described. An increased initial volume leads to an increased amplitude and propagation speed of the wave, until limiting values are reached. The same is true for the induced fluid velocity. The breaking of the waves, taking place in the form of the generation of vortices, becomes intense for the large waves. In this section detailed results for the velocity profiles and the vorticity in two different runs are presented, one for the almost largest wave, and one for the largest. Furthermore, the issues of limiting fluid velocity and broadening of the waves are considered, with results from several runs.

Run	Depth × length × width (m) (m) (m)	(Trapped volume) (l)	a_{12}/h_2	a_{23}/h_2	c_{12}/c_0	c_{23}/c_0	λ/h_2
A	0.4 × 0.5 × 0.5	(100)	1.05	0.97	1.60	1.57	9.5
B	0.4 × 0.75 × 0.5	(150)	1.23	1.20	1.77	1.76	12.4
C	0.375 × 1.25 × 0.5	(200)	1.25	1.25	1.78	1.67	12.6
D	0.4 × 1 × 0.5	(200)	1.23	1.20	1.71	1.75	14

TABLE 1. Trapped volume behind the gate prior to the experiment, and amplitude, speed and length of the largest waves. a_{12} and c_{12} are the average amplitude and speed between cameras 1 and 2. a_{23} and c_{23} the average amplitude and speed between cameras 2 and 3. Experiment as in figure 2(*a*).

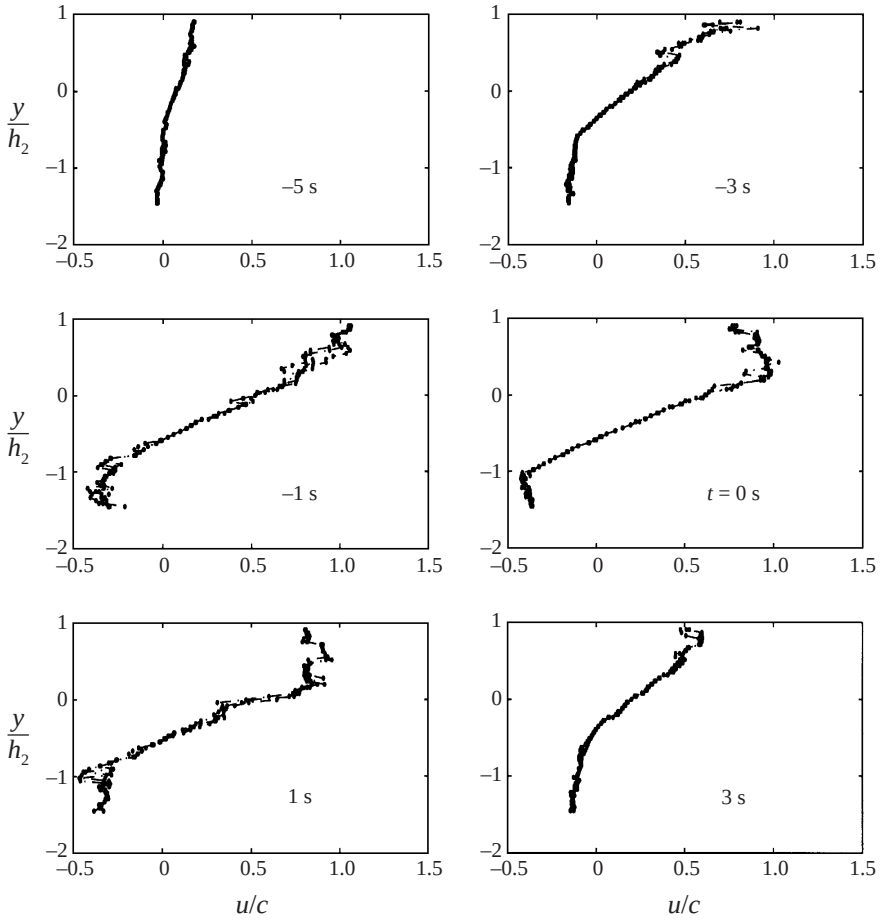

FIGURE 14. Time series of the horizontal velocity u vs. vertical coordinate y. PIV at camera 3. Initial volume 100 l^3 (run A in table 1).

7.1. *Velocity profiles*

Results from two typical runs, A and D in table 1, are given. The initial volumes are 100 dm^3 and 200 dm^3, respectively. The time-history of the horizontal velocity component $u(y;t)$ is obtained at the position of camera 3 (figures 14–15). The velocity is scaled by the wave speed c. The non-dimensional amplitude and propagation speed are given in table 1.

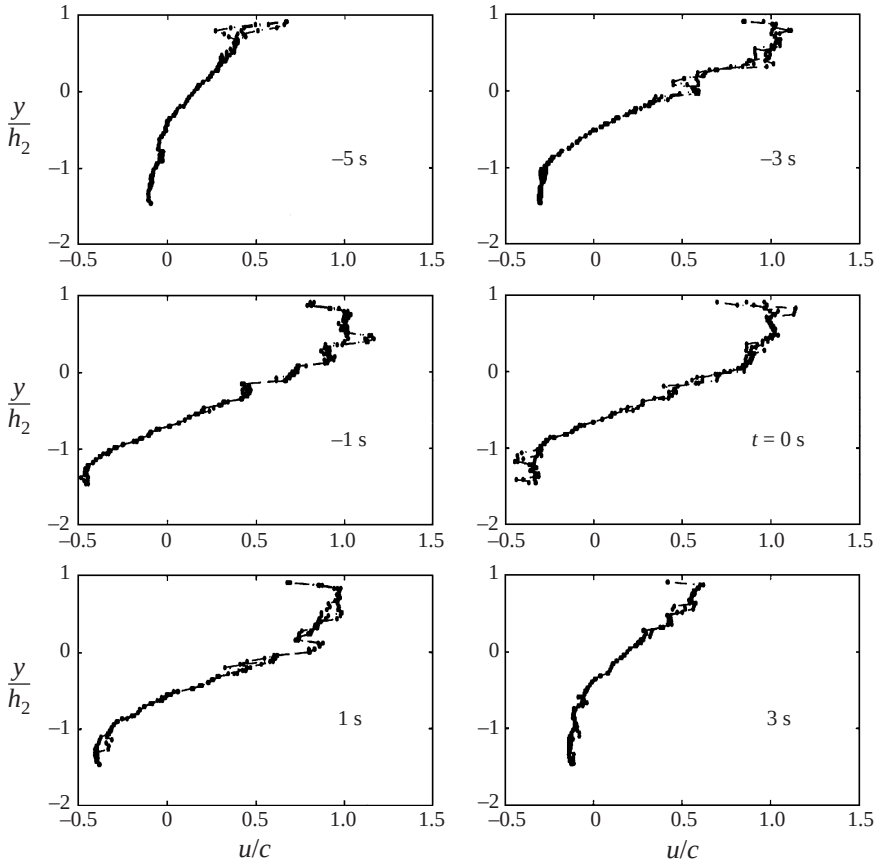

FIGURE 15. Same as figure 14, but initial volume 200 l (run D in table 1).

The measured fluid velocity close to the free surface in the centre of the wave is found to be comparable to the wave speed. More precisely, the fluid velocity in this region is $\boldsymbol{v} = c\boldsymbol{i} + \boldsymbol{v}'$, where $\boldsymbol{v}'$ contains small fluctuating velocities due to a number of vortices generated by the flow (figure 18). The magnitude of $\boldsymbol{v}'$ is small compared to the wave speed, i.e. $|\boldsymbol{v}'| \ll c$.

The velocity profile $u(y;t)$ is symmetric with respect to the centre of the wave when the amplitude is small (§ 5). The large-amplitude waves are not entirely symmetric, however. We believe the deviation from symmetry is caused by the non-symmetric presence of the large number of small vortices in the waves. While the two different runs have several features in common, there are also some important differences to be noted. The most visible difference is the time period between the arrival and disappearance of the wave at a given position of the tank. This is longer for the larger wave than for the smaller, despite the larger wave travelling faster than the smaller. This means that the wave with the larger initial volume is broader than the other. Secondly, the larger wave has a longer and somewhat thicker region in its upper part where the horizontal velocity is approximately equal to the propagation speed c.

7.2. *Vorticity*

The velocity fluctuations may be further examined by evaluating the vorticity component $\omega = \partial v/\partial x - \partial u/\partial y$ (figures 16–17). The vorticity component exhibits rather

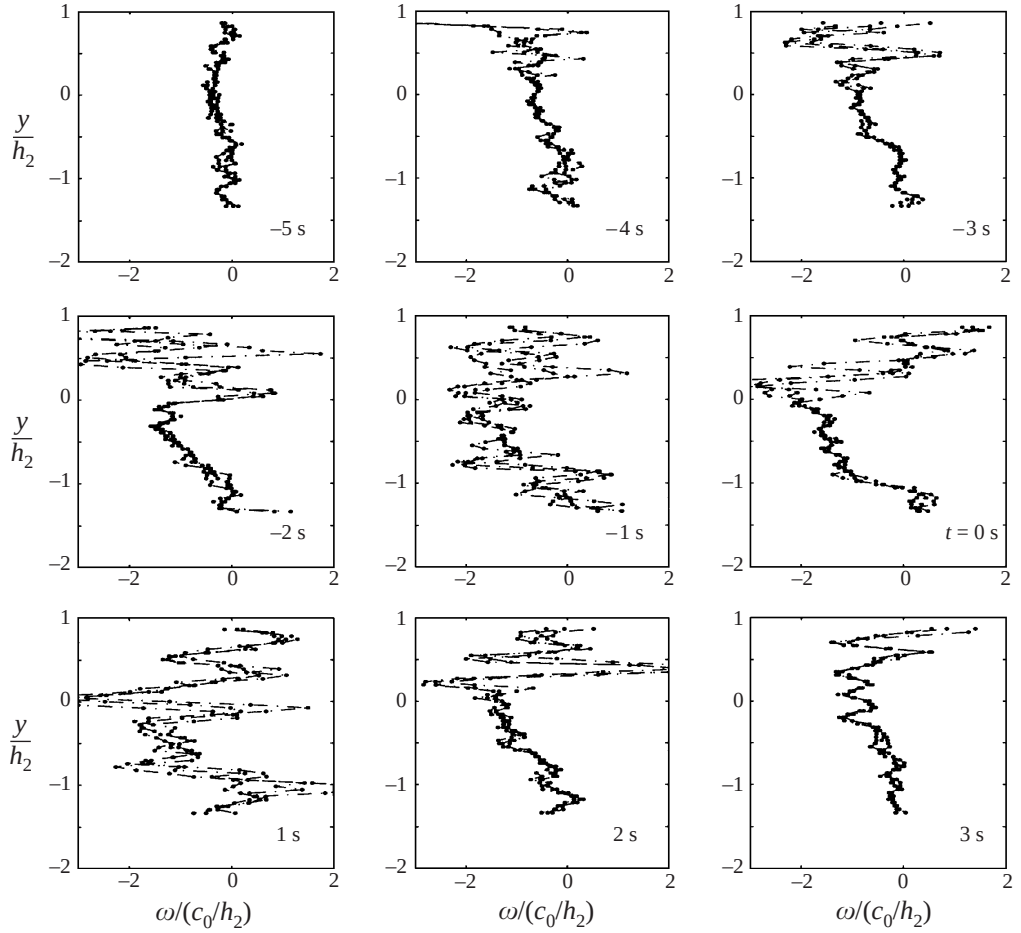

FIGURE 16. Time series of the vorticity $\omega = \partial v/\partial x - \partial u/\partial y$ vs. vertical coordinate y. PIV at camera 3. Initial volume 100 l (run A in table 1).

strong oscillations in the upper region of the wave where the velocity field has fluctuations. The vorticity oscillates about a non-zero mean. The oscillations illustrate the intensity and scale of the vortices which are generated in the leading part and above the centre of the wave, see also figure 18.

While the motion is two-dimensional for waves with small and moderate amplitude, three-dimensional effects take place for the largest waves. This is illustrated viewing the wave tank from above, recording the horizontal velocity field $u'\boldsymbol{i} + w\boldsymbol{k} = (u-c)\boldsymbol{i} + w\boldsymbol{k}$ just below the free surface; $w\boldsymbol{k}$ denotes the horizontal velocity component across the wave tank. Pronounced velocity fluctuations across the wave tank are found (figure 19). The vorticity component $\partial u/\partial z - \partial w/\partial x$, where z is the coordinate across the wave tank, is also shown in the figure. This vorticity component exhibits oscillations which are of the same size as for $\omega = \partial v/\partial x - \partial u/\partial y$. We have not been able to measure the vorticity component $\partial w/\partial y - \partial v/\partial z$. This requires equipment for three-dimensional PIV, which we do not have available.

7.3. *Broadening*

Figures 14–15 show that the waves broaden when their volume exceeds a certain value. The broadening effect is further illustrated in figure 20 (see also figure 3), where the

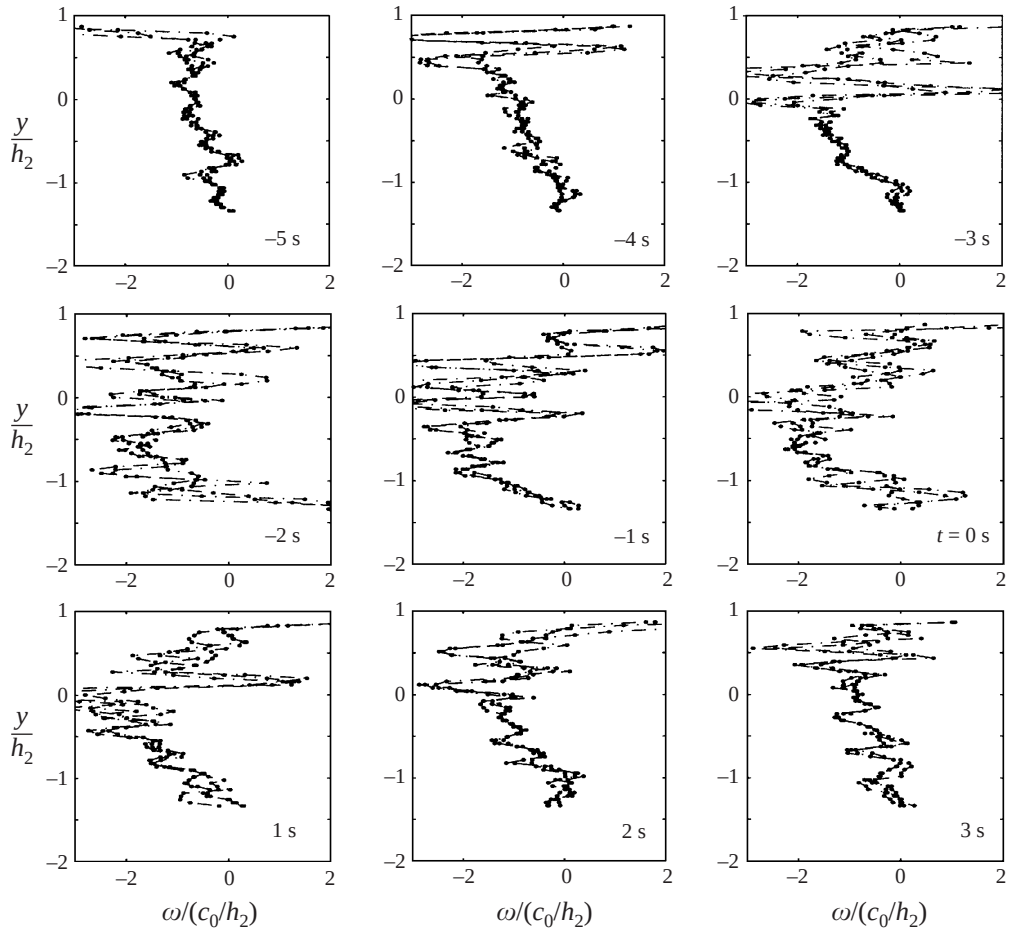

FIGURE 17. Same as figure 16, but initial volume 200 l (run D in table 1).

time history of the horizontal fluid velocity close to the free surface is displayed as function of time, for several initial volumes. Since the experimental velocity field contains fluctuations close to the free surface, and since the velocity estimates from the PIV analysis at the free surface are somewhat uncertain, we display the time history of the horizontal velocity averaged over a small vertical distance close to the free surface, i.e.

$$\overline{u}(t) = \int_{0.5h_2}^{0.9h_2} u(y,t)\,\mathrm{d}y \,/\, (0.4h_2)\,. \tag{7.1}$$

The results show that $\overline{u}_{max}$, defined as the maximal value of $\overline{u}(t)$ in each run, may become slightly larger than the propagation speed c of the wave. More precisely, we find after an initial phase, $\overline{u}_{max}/c \simeq 1.03$.

We also evaluate the wavelength as defined by

$$\lambda = \frac{1}{\overline{u}_{max}} \int_{-\infty}^{\infty} \overline{u}\,\mathrm{d}x = \frac{1}{\overline{u}_{max}} \int_{-\infty}^{\infty} \overline{u}(t)\,c\,\mathrm{d}t\,. \tag{7.2}$$

The theoretical and experimental results show that the wavelength decays with increasing amplitude ($\overline{u}_{max}/c$) for small and moderate waves (figure 21). There is

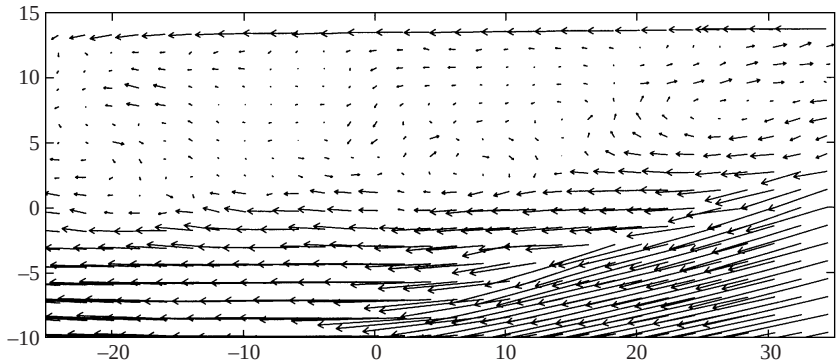

FIGURE 18. Velocity field $\boldsymbol{v} - c\boldsymbol{i}$. Close up of the region $-10 < y < 15$ cm below the free surface (at $y = 15$ cm). (For reference: the depth of the upper layer at rest is 15 cm.) Camera 3. Initial volume 200 l (run D in table 1).

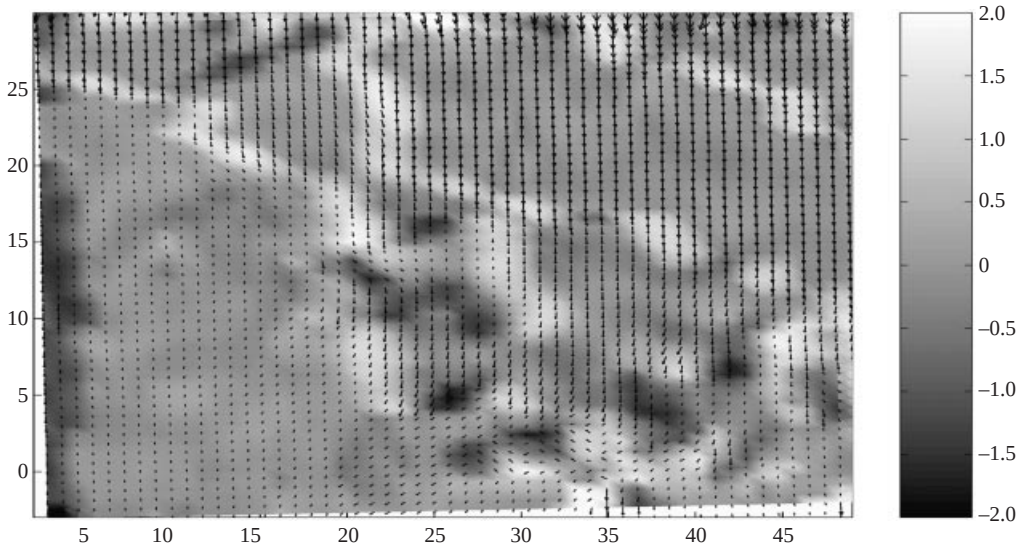

FIGURE 19. Horizontal velocity field $u\boldsymbol{i} + w\boldsymbol{k} - c\boldsymbol{i}$ at the free surface. Wave tank viewed from above. Vorticity component $(\partial u/\partial z - \partial w/\partial x)/(c_0/h_2)$ in grey scale. Initial volume 200 l (run D in table 1). Recording section 50 cm × 35 cm.

good agreement between experiments and theory for $\overline{u}_{max}/c$ less than about 0.9. The corresponding non-dimensional wave amplitude a/h_2 is then less than about 0.8. The experiments show, however, that the waves broaden when $\overline{u}_{max}/c$ becomes larger than about 0.9. The corresponding non-dimensional wave amplitude a/h_2 then exceeds 0.8, approximately. We recall that the theoretical model predicts that the maximal fluid velocity at the free surface exceeds the wave speed, and that a recirculating zone appears in the model, when a/h_2 exceeds the value of 0.855 (figure 22*b*). The corresponding theoretical $\overline{u}_{max}/c$ then exceeds 0.941. Thus, the departure of the experiments from the theory occurs for a wave amplitude where breaking of the waves can be anticipated from the former. From then on the theory and experiment exhibit rather different results. The broadening of the waves observed in the experiments is not found in the theory.

We note that the local breaking of the waves described in § 6.1 occurs when the

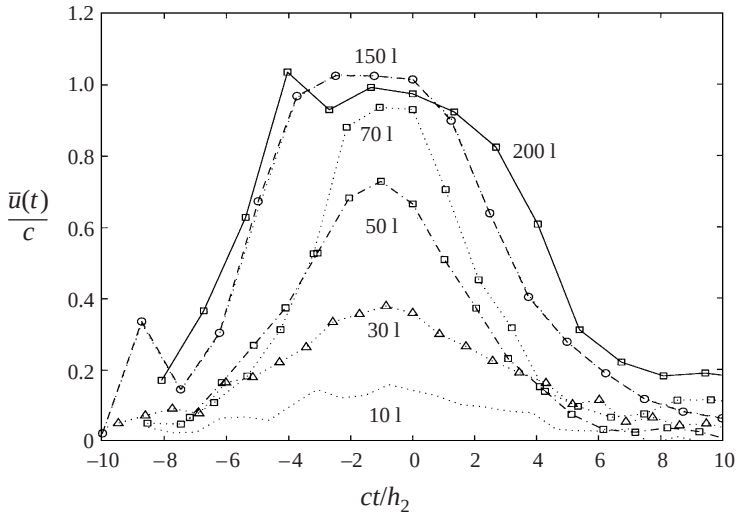

FIGURE 20. Broadening of the waves. $\bar{u}(t)/c$ vs. ct for the initial volumes shown (run D in table 1).

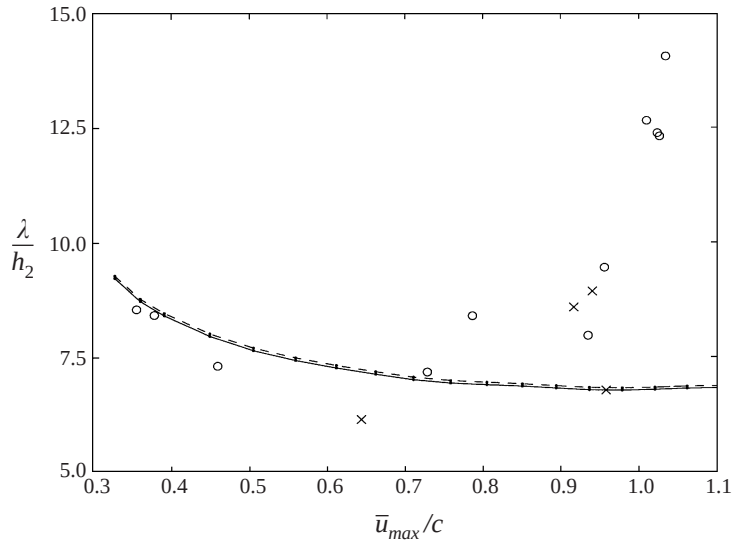

FIGURE 21. Wavelength λ as defined in (7.2) vs. $\bar{u}_{max}/c$. Experiments with model as in figure 2(*a*) (circles), model as in figure 2(*b*) (crosses) and theory (solid line). Also theoretical $\lambda = \int_{-\infty}^{\infty} u(y = h_2, t)\, c\, \mathrm{d}t / u(y = h_2)_{max}$ (dashed line). The black dots represent computational points.

maximal fluid velocity is somewhat smaller than c. More precisely, $|\boldsymbol{v}|_{max}$ is about 80% of c. The wavelength seems to be relatively insensitive to this local breaking, however.

Additional results for the largest waves are included in table 1, showing that the wave amplitude and speed become approximately the same for the 150 and 200 l waves. The 200 l wave in run D is longer than the 150 l wave, however. This suggests that the wave shapes in runs A–D are different, a result which also is evident from figures 3 and 20.

We may compare our results on this point with those of Stamp & Jacka (1995,

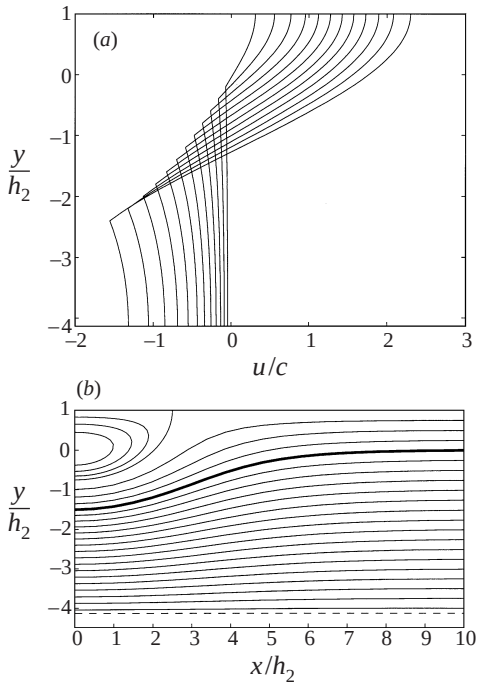

FIGURE 22. (*a*) Velocity profiles at wave crest for amplitudes $a/h_2 = 0.2, 0.4, 0.6, \ldots, 2.4$. (*b*) Streamlines for $a/h_2 = 1.5$. Thick line: the streamline between the upper and lower fluid. Dashed line: bottom. $h_1/h_2 = 4.13$.

§4.3). They obtained a linear relationship between a typical wavelength and the wave amplitude in their experiments for waves with large amplitude. They noted that all waves of non-dimensional amplitude larger than one were similar in shape and differed only by a scaling factor. Further, they found that their measurements were consistent with the fully nonlinear theory by Tung *et al.* (1982) and suggested that the behaviour of the waves could be accounted for by higher-order amplitude terms without taking into account viscous effects. Our findings are different on this point, as just discussed.

7.4. *Maximal amplitude and wave speed in the experiments*

We have experimentally found that the fluid velocity is bounded by the wave speed i.e. $|\boldsymbol{v}|_{max} \sim c$. We also find maximal values of the wave speed and amplitude in the experiments. These maximal values are obtained with different initial volumes (table 1). We do not exclude the possibility that waves with larger amplitude may be generated with another experimental arrangement, one with a relatively deeper and longer wave tank. Still we expect generally that the fluid velocity in the centre of a large wave is of the form $\boldsymbol{v} = c\boldsymbol{i} + \boldsymbol{v}'$ where $|\boldsymbol{v}'| \ll c$. Waves with larger amplitude and speed than found in the present experiments are expected to have a relatively larger volume with a fluid velocity of this form.

We note that Stamp & Jacka, in their experiments with solitary waves of mode 2, were able to generate waves with amplitude up to about three times the characteristic depth of the stratified layer. Further, they note that other investigators using their experimental facility were able to make waves with a non-dimensional amplitude as large as about five.

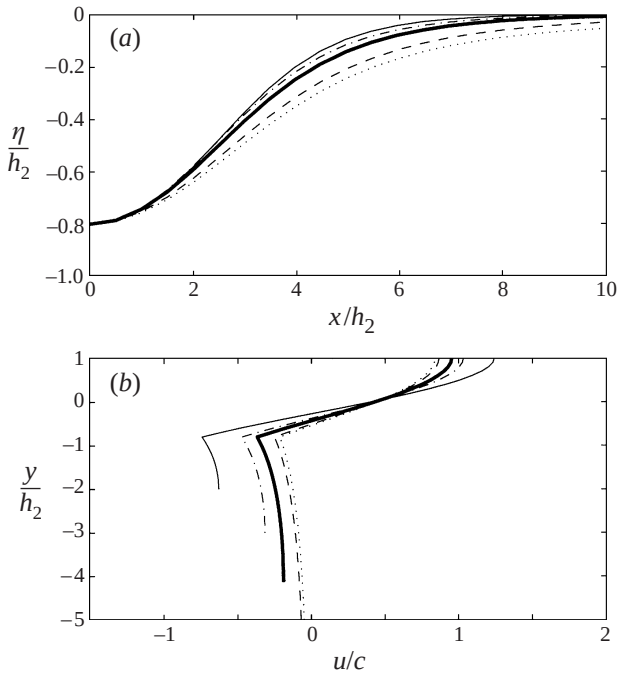

FIGURE 23. Theoretical results for the line η separating the layers (a) and theoretical velocity profiles at the crest (b) for different depth ratios: $h_1/h_2 = 2$ (thin solid line), 3 (dash-dot line), 4.13 (thick solid line), 10 (dashed line) and 100 (dotted line).

As mentioned in the Introduction, the Reynolds number in our experiments, based on the thickness of the thinner layer, covers the range 10^4–3×10^4, while the Reynolds number in the experiments by Stamp & Jacka covers the range about 36–70. The qualitatively different results of the two experiments may, perhaps, be explained by the differences in scale.

8. Supplementary theoretical results

Several theoretical results have been presented in the previous sections. It may be relevant to present a few supplementary computations in order to highlight certain aspects of in the two-layer model and to briefly discuss solitary wave properties not previously mentioned.

First, the velocity profile at the maximal depression of the wave is considered. The numerical results show that u/c increases almost linearly with the wave amplitude. The fluid velocity at the free surface in the centre of the wave, i.e. $u(x = 0, y = h_2)$, becomes equal to the wave speed when $a/h_2 = 0.855$. In figure 22(a) computations of u/c as large as 2.3 at the free surface are shown. The amplitude is then $a/h_2 = 2.4$. The computations may be pursued for larger waves. In view of the experimental results, however, no such attempts are made, since the theoretical results with $u/c > 1$ are quite unrealistic. For amplitudes in excess of $a/h_2 = 0.855$ the theoretical model predicts a region with recirculation close to the free surface (figure 22b). No additional assumptions are made to compute this flow: the prescribed amplitude of the wave is just increased stepwise in the computations. Noting that the streamlines and lines of constant density in the model coincide, the predicted flow with recirculation contains

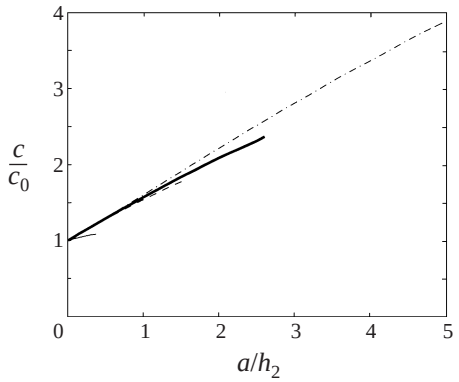

FIGURE 24. c/c_0 for various depth-ratios: h_1/h_2 =0.5 (thin solid line), 3 (dashed line), 4.13 (solid line), 10 (dash-dotted line).

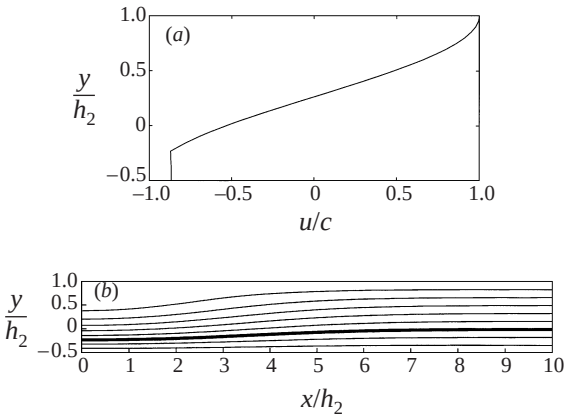

FIGURE 25. Solitary wave of depression for $h_1/h_2 = 0.5$. (*a*) Velocity profile at maximal depression. (*b*) Streamlines.

fluid with higher density inside the vortex than at the separating streamline. The latter has the same density as the streamline at the free surface ($y = h_2$). In view of the experimental findings, the computations illustrate that the model is appropriate until recirculation occurs. An exception, however, is the breaking discussed in § 6.1.

We have so far described a detailed experimental and theoretical investigation for only one ratio between the depths of the layers, i.e. $h_1/h_2 = 4.13$. Other ratios may be investigated computationally. The results in figures 23–24 show that the velocities close to the free surface are rather similar for all h_1/h_2 larger than about 3. For h_1/h_2 decreasing below about 2, keeping the wave amplitude fixed, the value of u/c at the free surface increases rather rapidly (figures 23, 25).

The wave speed is also found to be rather independent of h_1/h_2 when the latter is larger than about 3 and u/c is less than unity. In this parameter range, the nonlinear wave speed increases approximately linearly with amplitude (figure 24).

In a two-layer fluid with a constant density in each layer, solitary waves of depression or elevation may propagate if $h_1^2\rho_2 - h_2^2\rho_1$ is larger or smaller than zero, respectively. Here, h_1 and ρ_1 denote depth and density of the lower layer, while h_2 and ρ_2 denote depth and density of the upper. In the present two-layer model, however, a solitary wave always exhibits an excursion out of the layer with linear

stratification (figure 25). This is true for the wave mode with largest speed as can be anticipated from equation (3.20). Observations in the wave tank confirm the computations (results not shown). Figure 25 exhibits pronounced excursions of the streamlines that are close to the free surface in the far field. The wave speed has very weak amplitude dependence when $h_1 < h_2$ (figure 24).

The polarity of solitary waves may alternatively be determined from the sign of the coefficient of the nonlinear term in weakly nonlinear KdV or 'finite depth' theory. This coefficient is given in e.g. Apel *et al.* (1985, equations (4)–(5)), from which we obtain

$$\frac{3c_0}{2}\int_{-h_1}^{h_2}(\hat{\psi}_y)^3\mathrm{d}y \Big/ \int_{-h_1}^{h_2}(\hat{\psi}_y)^2\mathrm{d}y = \frac{aN_0c_0|\sin(2N_0h_2/c_0)|}{\cos^2(N_0h_2/c_0)+h_2/h_1}, \tag{8.1}$$

where $\hat{\psi}$ is obtained in (3.18)–(3.19), with $\psi(x,y) = \hat{\psi}(y)\cos\nu x$. The value of (8.1) is positive for the stratification (3.9), for $0 < h_2/h_1 < \infty$. (The weakly nonlinear models are included in the fully nonlinear method described in § 3.)

9. Concluding remarks

The characteristic properties of solitary waves propagating in a stratified fluid are investigated combining experiments and theory. In most of the experiments the fluid has a shallow upper layer with a linear stratification and a deep lower layer with constant density. These experiments are motivated by conditions in nature where solitary waves of depression are observed (Farmer & Smith 1980; Apel *et al.* 1985). Some of the experiments are performed with an inverted model where a thin lower layer with linear stratification is underlying a thick layer of constant density. In these experiments solitary waves of elevation are investigated. Particle tracking velocimetry (PTV) and particle image velocimetry (PIV) provide recordings of the quite detailed behaviour of the induced velocities of the waves. The propagation speed of the waves is also determined.

The accuracy of the PTV recordings was analysed by Grue *et al.* (1999) who found that this was always better than about 7–8% relative to the linear long-wave speed. This analysis is also valid here. A corresponding accuracy applies for the PIV recordings.

A fully nonlinear theoretical and numerical model complementary to the experiments is developed. This is a two-layer model where a thin layer of linearly stratified fluid has constant Brunt–Väisälä frequency and a thick layer has zero Brunt–Väisälä frequency. The density at the boundary between the two fluids is continuous. This is also true for the fluid velocity. (The model may be generalized to include a jump in the density and the fluid velocity at the boundary between the fluids.) Wave solutions are obtained by means of integral equations.

Particular attention is paid to the role of the breaking of the waves observed in the experiments. For the large waves, the breaking occurs in a region in the centre of the waves, in the thin layer with linearly stratified fluid. The breaking limits the fluid velocity. The latter, in the region with breaking, is found to be of the form $\boldsymbol{v} = c\boldsymbol{i} + \boldsymbol{v}'$ where $c\boldsymbol{i}$ denotes the wave velocity and $\boldsymbol{v}'$ a velocity field where $|\boldsymbol{v}'| \ll c$. This means that the wave speed approximately provides an upper bound for the fluid velocity induced by the wave. Breaking occurs similarly in the experiments with the inverted two-layer model, when the waves are large. A fluid velocity approximately equal to the wave speed means that the wave transports mass, which has implications for transportation of water masses, sediments and larvae in the ocean. A similar mass transport due to solitary waves may also take place in the atmosphere.

The experimental and theoretical velocity fields exhibit, generally speaking, good agreement up to breaking. Intensive breaking is found to occur for a wave amplitude a less than about 0.8 times the depth h_2 of the linearly stratified layer. This is in agreement with the theoretical model which predicts an induced fluid velocity being less than the wave speed when $a/h_2 < 0.855$. For larger waves the theory does not fit with the experimental observations. We find that the experimental waves broaden when the non-dimensional wave amplitude exceeds 0.8–0.9. The experiments suggest that the broadening is caused by the wave breaking which limits the magnitude of the fluid velocity. The broadening is not reproduced by the theory. The broadening effect found here is entirely different from the one taking place in a two-fluid system with constant densities in each of the layers. In the latter case, the limiting amplitude and wave speed, and thereby the broadening of the waves, are determined by the finite total depth of the fluid (Amick & Turner 1986; Turner & Vanden-Broeck 1988). The limiting amplitude, wave speed and fluid velocity are confirmed experimentally (Grue *et al.* 1999).

The maximal amplitude in our experiments is approximately 1.25 times the depth of the linearly stratified layer, while the maximal propagation speed is approximately 1.78 times the linear long-wave speed. The maximal values are obtained with different initial volumes (table 1). We note that waves with larger amplitude may possibly be generated in a deeper and longer tank. However, we still generally expect that the fluid velocity will be bounded by the wave speed, i.e. $\boldsymbol{v} = c\boldsymbol{i} + \boldsymbol{v}'$ where $|\boldsymbol{v}'| \ll c$.

Most of our experiments are performed with a thin stratified fluid above a thick homogeneous fluid. For moderately large waves, we observe in these experiments that local breaking takes place by the formation of vortices in the leading part of the waves close to the free surface. These waves have smaller amplitude than the waves with intense breaking, where the maximal fluid velocity at the free surface is about 80% of the wave speed. The corresponding wave amplitude is about 0.65 times the depth h_2 of the linearly stratified layer. We have in a few experiments also observed this local breaking for a wave amplitude as small as $a/h_2 \simeq 0.5$. Additional experiments with the inverted two-layer model suggest that the local breaking depends on the boundary conditions at the free surface and that the effect of a surface film may be the cause of the breaking (§ 6.2). We may speculate that a similar breaking may occur for solitary waves at large scale. Wind stress on the ocean surface may, perhaps, cause breaking of moderately large waves in a similar way to that described here.

We compare our results with those of Stamp & Jacka (1995) who performed experiments with solitary waves of mode 2 propagating on a thin pycnocline between two deep layers of constant densities. The half-thickness of the pycnocline was 2.8 mm. Thus the length scale in our experiments is about 50 times larger than the length scale in their experiments. Further, the Reynolds number based on the thickness of the thinner layer in our experiments is in the range 10^4–3×10^4 while theirs is in the range of about 36–70. Thus, there are important differences between our experiments and theirs. A few of the results may be compared, however. We find, like them, a linear relationship between the wave speed and amplitude. This relationship is found both from experiments and from fully nonlinear theory (Tung *et al.* 1982; present theory). Stamp & Jacka also quantified a typical length scale of the waves, finding a linear relationship between the wavelength and the amplitude when the waves were large. They further commented that the large waves were of similar shape, differing only by a scaling factor, and that the measurements were consistent with the fully nonlinear theory by Tung *et al.* (1982), which predicts a recirculating zone for the large waves similar to the computations in figure 22. They suggested that the behaviour of the

waves can be accounted for by higher-order amplitude terms without taking account of viscous effects.

On this point our experimental results are fundamentally different from theirs. The broadening of the waves found here occurs when intense wave breaking is observed in the experiments and the velocity field in the core of the wave is of the form $\boldsymbol{v} = c\boldsymbol{i} + \boldsymbol{v}'$ with $|\boldsymbol{v}'| \ll c$. The fully nonlinear inviscid theory cannot explain the observed broadening of the waves. An explanation of the different results may be the value of the Reynolds number in the experiments.

The results here lead us to expect that large-amplitude solitary waves of mode 2 have a core where the velocity field is of a similar form to the mode 1 waves investigated here, when the Reynolds number is large. Mode 2 waves are expected to broaden similarly to the mode 1 waves discussed here.

Focus is here on the generation of a single solitary wave in the experiments. This is achieved by a careful adjustment of the depth and length of a trapped volume of fluid in the wave tank. We are able to generate a single solitary wave even for trapped fluid with very large volume. This is true also for a two-layer fluid with constant density in the layers, see Grue *et al.* (1999). This is, however, not in conflict with a generation of a train of solitary waves, see e.g. Maxworthy (1980), and Kao, Pan & Renouard (1985). In the latter case the trapped volume has a relatively longer horizontal extent and is relatively shallower. For shallow trapped fluid, the results of inverse scattering theory should be relevant.

Solitary waves in the present two-layer model have much in common with their counterpart in a two-layer model with constant density in each of the layers. There are, however, several important differences to be noted. Solitary waves in the present two-layer fluid are in brief characterized by: the fluid velocity may become equal to and even slightly exceed the wave speed; there is always an excursion of the waves into the layer with constant density (the longest wave mode), a result which is true for any ratio between the depths of the layers; there is an approximately linear relationship between wave speed and amplitude; convective breaking and broadening of the waves occur when the fluid velocity becomes comparable to the wave speed; the waves may transport mass; in the present experiments wave breaking is also observed for a fluid velocity about 80% of c.

In a two-layer model with constant density in each of the layers solitary waves are characterized by: waves of depression or elevation if $h_1^2\rho_2 - h_2^2\rho_1$ is larger or smaller than zero, respectively, where h_1, h_2, ρ_1, ρ_2 are defined in the text at the end of § 8; breaking due to shear instability may occur at the pycnocline; there is a nonlinear relationship between the wave speed and the amplitude; limiting values of the amplitude, wave speed and fluid velocity exist; the fluid velocity is always less in magnitude than the wave speed; the waves may not transport mass; broadening occurs when maximal wave speed and amplitude are reached.

This work was conducted under the Strategic University Programme 'General Analysis of Realistic Ocean Waves' funded by the Research Council of Norway. The discussions with Alexander Korobkin, Howell Peregrine, Jan Erik Weber and Deborah J. Wood, and the technical assistance by Arve Kvalheim and Svein Vesterby are gratefully acknowledged.

REFERENCES

Amick, C. J. & Turner, R. E. L. 1986 A global theory of internal solitary waves in two-fluid systems. *Trans. Am. Math. Soc.* **298**, 431.

Apel, J. R., Holbrook, J. R., Liu, A. K. & Tsai, J. 1985 The Sulu Sea internal soliton experiment. *J. Phys. Oceanogr.* **15**, 1625.

Brown, D. J & Christie, D. R. 1998 Fully nonlinear solitary waves in continuously stratified incompressible Boussinesq fluids. *Phys. Fluids* **10**, 2569.

Dalziel, S. B. 1992 Decay of rotating turbulence: some particle tracking experiments. *Appl. Sci. Res.* **49**, 217.

Davis, R. E. & Acrivos, A. 1967 Solitary internal waves in deep water. *J. Fluid Mech.* **29**, 593.

Dold, J. W. & Peregrine, D. H. 1985 An efficient boundary-integral equation method for steep unsteady water waves. *Numerical Methods for Fluid Dynamics*, vol. 2 (ed. K. W. Morton & M. J. Baines), pp. 671–670. Clarenden.

Duda, T. & Farmer, D. M. 1998 (Eds.), IOS/WHOI/ONR Internal Solitary Wave Workshop, Victoria B.C., Canada. *Woods Hole Oceanographic Institution Tech. Rep. WHOI*-99-07. http://www.whoi.edu/science/AOPE/ISW98workshop.

Farmer, D. M. & Smith, J. D. 1980 Tidal interaction of stratified flow with a sill in Knight Inlet. *Deep-Sea Res.* **27A**, 239.

Grue, J., Friis, A., Palm, E. & Rusås, P.-O. 1997 A method for computing unsteady fully nonlinear interfacial waves. *J. Fluid Mech.* **351**, 223.

Grue, J., Jensen, A., Rusås, P.-O. & Sveen, J. K. 1999 Properties of large amplitude internal waves. *J. Fluid Mech.* **380**, 257.

Kao, T. W., Pan, F.-S. & Renouard, D. 1985 Internal solitons on the pycnocline: generation, propagation, and shoaling and breaking over a slope. *J. Fluid Mech.* **159**.

Long, R. R. 1958 Tractable models of steady-state stratified flow with shear. *Q. J. R. Met. Soc.* **84**, 159.

Maxworthy, T. 1980 On the formation of nonlinear internal waves from the gravitational collapse of mixed regions in two and three dimensions. *J. Fluid Mech.* **96**, 47.

Raffel, M., Willert, C. & Kompenhans, J. 1998 *Particle Image Velocimetry*. Springer.

Simpson, J. E. & Britter, R. E. 1979 The dynamics of the head of a gravity current advancing over a horizontal surface. *J. Fluid Mech.* **94**, 477.

Stamp, A. P. & Jacka, M. 1995 Deep-water internal solitary waves. *J. Fluid Mech.* **305**, 347.

Sveen, J. K. 1998 An introduction to MatPIV v.1.1. Documentation and code: http://www.math.uio.no/~jks.

Tung, K. K., Chan, T. F. & Kubota, T. 1982 Large amplitude waves of permanent form. *Stud. Appl. Maths* **16**, 1.

Turkington, B., Eydeland, A. & Wang, S. 1991 A computational method for solitary internal waves in a continuously stratified fluid. *Stud. Appl. Maths* **85**, 93.

Turner, R. E. L. & Vanden-Broeck, J.-M. 1988 Broadening of interfacial solitary waves. *Phys. Fluids* **31**, 372.

Westerweel, J., Dabiri, D. & Gharib, M. 1997 The effect of a discrete window offset on the accuracy of cross-correlation analysis of digital PIV recordings. *Exps. Fluids* **23**, 20.

Willert, C. E. & Gharib, M. 1991 Digital particle image velocimetry. *Exps. Fluids* **10**, 181.

Yih, C.-S. 1960 Exact solutions for steady two-dimensional flow of a stratified fluid. *J. Fluid Mech.* **9**, 161.